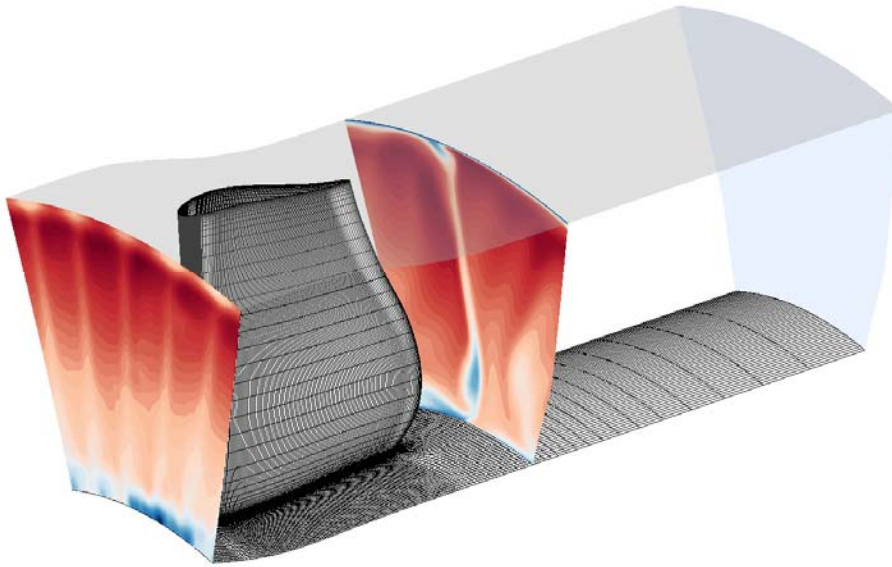




CHALMERS
UNIVERSITY OF TECHNOLOGY



Master's thesis in

Modeling of laminar-turbulent transition in a turbine rear structure

DIEGO AUGUSTO ARIAS
SHAMEEK DEV ROY

DEPARTMENT OF MECHANICS AND MARITIME SCIENCES
CHALMERS UNIVERSITY OF TECHNOLOGY

Gothenburg, Sweden 2021
www.chalmers.se

MASTER'S THESIS IN

Modeling of Laminar-Turbulent Transition in a Turbine Rear Structure

DIEGO AUGUSTO ARIAS
SHAMEEK DEV ROY

Department of Mechanics and Maritime Sciences
Division of Fluid Mechanics

CHALMERS UNIVERSITY OF TECHNOLOGY
Göteborg, Sweden 2021

Modeling of Laminar-Turbulent Transition in a Turbine Rear Structure
DIEGO AUGUSTO ARIAS
SHAMEEK DEV ROY

© DIEGO AUGUSTO ARIAS, 2021-06-30
© SHAMEEK DEV ROY, 2021-06-30

Master's Thesis 2021:51
Department of Mechanics and Maritime Sciences
Division of Fluid Mechanics

Chalmers University of Technology
SE-412 96 Göteborg
Sweden
Telephone: + 46 (0)31-772 1000

Cover:
Total Pressure Distribution at Inlet and Evaluation Plane of the OGV Domain

Department of Mechanics and Maritime Sciences
Göteborg, Sweden 2021-06-30

Modeling of Laminar-Turbulent Transition in a Turbine Rear Structure
DIEGO AUGUSTO ARIAS
SHAMEEK DEV ROY
Department of Mechanics and Maritime Sciences
Division of Fluid Mechanics
Chalmers University of Technology

Abstract

The turbine rear structure (TRS) of modern aircraft gas turbine engines have several significant role, one of which is de-swirling the outlet flow coming from the Low Pressure Turbine (LPT) located upstream. Furthermore, the Outlet Guide Vane (OGV) in the TRS provides a structural support between the aft bearing support and main engine case. Other than de-swirling the flow, the TRS-OGV is mechanically and thermally loaded due to the hot outlet gases coming from LPT, which requires the OGV to be designed robustly. The TRS facility in Chalmers University, has a capability of operating over a wide range of Reynolds number, which allows several modes of transition, which in turn affects the aerodynamic and aerothermal performance. This thesis presents a tuned case-specific numerical investigation on the laminar-turbulent transition flow structures in the Turbine Rear Structure- Outlet Guide Vane (TRS-OGV). The work includes the processes and results of matching the laminar turbulent transition in the TRS OGV using RANS-CFD with SST $k-\omega$ turbulence model and the Langtry-Menter $\gamma-\theta$ transition model. Experimental data for a certain case was used for ambient and boundary conditions for the inlet, outlet, turbulence decay and surface heat transfer. The numerical results obtained, match the experimental verification data considerably well.

Key words: Blade Loading, Boundary Layer, Heat Transfer Coefficient, Momentum Thickness Reynolds Number, Outlet Guide Vane, Swirl Angle, Transition Onset, Turbulent Decay, Turbulent Intensity, y^+ .

Contents

Abstract	I
Contents.....	II
Table of Figures.....	IV
Acknowledgements	VI
Notations.....	VII
1 Background.....	1
2 Introduction.....	2
3 Theoreticals explanations.....	5
3.1 OGV airfoil geometry.....	5
3.2 Laminar/transitional/turbulent boundary regions	5
3.3 Heat transfer coefficient.....	7
3.4 Y^+ dimensionless wall distance.....	8
3.5 Turbulent and transitional models.....	9
3.5.1 $k - \epsilon$ model.....	10
3.5.2 $k - \omega$ model	12
3.5.3 SST (Shear Stress Transport) model.....	13
3.5.4 $\theta - \gamma$ Transition model (linked with SST model).....	15
3.5.4.1 Transition theory.....	15
3.5.4.2 Transition onset.....	16
3.5.4.3 Transport equations.....	17
3.6 Heat transfer modelling.....	21
4 Methodology	22
4.1 Experimental data	22
4.2 Processing of experimental data.....	24
4.3 Numerical simulations	26
4.3.1 Geometry.....	26
4.3.2 Mesh.....	27
4.3.3 Numerics.....	29
4.3.3.1 Boundary conditions.....	29
4.3.3.2 Inlet and Outlet initial conditions	29
4.3.3.3 Analysis type	30
4.3.3.4 Turbulent and transitional model.....	30
4.3.4 Run and Mesh Independence Study	30

5	Results	42
5.1	Aerodynamic evaluation.....	42
5.1.1	Inlet	42
5.1.1.1	Swirl angle	42
5.1.1.2	Total pressure and total pressure coefficient	44
5.1.2	Blade loading.....	46
5.1.3	Outlet	48
5.1.3.1	Swirl angle	48
5.1.3.2	Total pressure and total pressure coefficient	51
5.1.3.3	Wakes	53
5.1.4	Turbulence decay at freestream	55
5.1.5	Transition onset (aerodynamic evaluation).....	57
5.1.5.1	Suction side	57
5.2	Aerothermal evaluation.....	59
5.2.1	Heat transfer coefficient over the blade	59
5.2.2	Transition onset (aerothermal)	60
5.2.2.1	Suction side	60
6	Conclusions	62
7	Future work.....	63
8	Bibliography	64

Table of Figures

Figure 1. Chalmers OGV-LPT facility (I. Jonsson V. C., 2020)	2
Figure 2. GP7000 turbofan engine, from (B.Rojo, 2017). TRS-OGV highlighted	3
Figure 3. Cross-Section of TRS Source: (B.Rojo, 2017).....	4
Figure 4. OGV blade shape from (B.Rojo, 2017). Airflow from left to right	5
Figure 5. Heat Transfer behaviour in the boundary layer (Lienhard, 2020).....	6
Figure 6. Natural Transition Process (A.A.Torres Sampaio Barros, 2017).....	6
Figure 7, Momentum Thickness Explanation (CFDSupport, s.f.).....	16
Figure 8. Coefficients gamma theta equations (for Py_1 , Py_2 and Ey_2 equations)	18
Figure 9. Comparison of expected results for the 2 simplifications	21
Figure 10. Location of pressure taps, reference probe and evaluation planes	22
Figure 11. OGV blade with 77 pressure taps and channels (B.Rojo, 2017).....	23
Figure 12. Extended Experimental Grid (blue) vs Virtual Grid (orange) Inlet Plane..	25
Figure 13. Extended Experimental Grid (blue) vs Virtual Grid (orange) Eval. Plane.	25
Figure 14. Ansys Workbench layout	26
Figure 15. TRS-OGV on Design Modeler	27
Figure 16. TurboGrid mesh final result (7,1 million elements).....	28
Figure 17. Symmetry planes at 2 blades domain	28
Figure 18. Convergence of Wall HTC Average value (constant temperature).....	32
Figure 19. Convergence of Wall HTC Average value (constant wall heat flux).....	33
Figure 20. Convergence of y^+ Average value (constant temperature)	34
Figure 21. Convergence of y^+ Average value (constant wall heat flux)	35
Figure 22. Evolution of Area Average HTC (constant temperature).....	36
Figure 23. Evolution of Area Average HTC (constant heat flux).....	36
Figure 24. Evolution of y^+ (constant temperature).....	37
Figure 25. Evolution of y^+ (constant heat flux).....	37
Figure 26. Imbalances (constant temperature).....	38
Figure 27. Imbalances (constant wall heat flux).....	38
Figure 28. Evolution mass and momentum residuals (constant temperature)	39
Figure 29. Evolution mass and momentum residuals (constant wall heat flux)	39

Figure 30. Evolution heat transfer and turbulent residuals (constant temperature).....	40
Figure 31. Evolution heat transfer and turbulent residuals (constant wall heat flux) ..	40
Figure 32. Evolution transitional residuals (constant temperature)	41
Figure 33. Evolution transitional residuals (constant wall heat flux)	41
Figure 34. Swirl Angle at Inlet plane (Experimental).....	43
Figure 35. Swirl Angle implementation on the numerical domain.....	43
Figure 36. Graph comparing Swirl Angle at Inlet (CFD refers to interpolated).....	44
Figure 37. Total Pressure at Inlet plane (Experimental)	45
Figure 38. Total Pressure implementation on the numerical domain	45
Figure 39. Total Pressure Coefficient comparison at Inlet	46
Figure 40. Blade loading comparison at 25% span.....	47
Figure 41. Blade loading comparison at 50% span.....	47
Figure 42. Blade loading comparison at 75% span.....	48
Figure 43. Swirl Angle at Outlet plane (Experimental)	49
Figure 44. Swirl Angle at Outlet plane (Numerical).....	49
Figure 45. Graph comparing Swirl Angle at Outlet.....	50
Figure 46. Total Pressure at Outlet plane (Experimental)	51
Figure 47. Total Pressure at Inlet plane (Numerical).....	52
Figure 48. Total Pressure Coefficient comparison at Outlet.....	53
Figure 49. Wake analysis at Outlet plane (Experimental)	54
Figure 50. Wake analysis at Inlet plane (Numerical)	54
Figure 51. Turbulence Decay, first approach.....	55
Figure 52. Turbulence Decay with different Length scales	56
Figure 53. HTC Comparison at Suction Side with different Intensities	57
Figure 54. HTC Comparison at Suction Side with different length scales	58
Figure 55. HTC profile at the Suction Side	59
Figure 56. Experimental HTC profile at Suction Side (I. Jonsson V. C., 2020)	59
Figure 57. HTC profile at the Pressure Side (Numerical)	60
Figure 58. Experimental HTC profile at Pressure Side (I. Jonsson V. C., 2020)	60
Figure 59. Heat Transfer Coefficient Comparison at Suction Side with Constant wall temperature and constant heat flux on the Blade wall	61

Acknowledgements

Any project big or small is successful largely due to the efforts of a number of wonderful people who have always given their valuable advice or lent a helping hand. We sincerely appreciate the inspiration support and guidance of all those people who have been instrumental in making this thesis project a success.

We are highly grateful to Carlos Xisto who in spite of being extraordinarily busy with his duties, took time to hear our obligation providing this wonderful opportunity to do a master thesis project in the department of Mechanics and Maritime Sciences.

Our sincere thanks to Marcus Lejon, Oliver Sjogren and Vinícius Tavares Silva for their excellent suggestions and advice throughout the project.

We extend our profound gratitude to Isak Jonsson, our mentor for guidance, who has indeed been a polestar throughout the duration of the project. His light of enthusiasm, knowledge and his invaluable insights has been a driving force to this endeavor. We thank them for giving us full support to complete our project successfully.

We would also extend our regards to thank all the our friends and family for their immense support during the hectic time to bringing out this project to complete successfully.

Göteborg March 2021-06-30

SHAMEEK DEV ROY
DIEGO AUGUSTO ARIAS

Notations

Acronyms

BSL	BaSeLine model
CAD	Computer Aided Design
CFD	Computational Fluid Dynamics
HTC	Heat Transfer Coefficient
LPT	Low Pressure Turbine
NGV	Nozzle Guide Vane
OGV	Outlet Guide Vane
RANS	Reynolds Average Navier-Stoke
RMS	Root Mean Square
SST	Shear Stress Transport
TRS	Turbine Rear Structure

Roman upper case letters

C_f	Friction coefficient
C_{p0}	Total pressure coefficient
C_p	Static pressure coefficient
\overline{D}_k	Modified turbulence dissipation term due to viscous forces
E_{y1}	Intermittency sinks
E_{y2}	Relaminarization sinks
F_1	Switching model blending function SST model
F_2	Eddy-viscosity blending function SST model
\tilde{F}_1	Switching model blending function $\theta - \gamma$ model
$F_{\theta t}$	Theta sinks
F_{length}	Empirical function for length of the transitional region
F_{onset}	Switching intermittency function
F_{onset1}	Auxiliar switching intermittency function 1
F_{onset2}	Auxiliar switching intermittency function 2
F_{onset3}	Auxiliar switching intermittency function 3
L	Reference length for Reynold's calculations (0,2 m)
$P_{\theta t}$	Theta sources
P_k	Turbulent production due to viscous forces
\overline{P}_k	Modified turbulent production term due to viscous forces
P_s or p	Static pressure
$P_{s,Pitot}$	Static Pitot pressure
P_t	Total pressure
$P_{t,Pitot}$	Total Pitot pressure
P_{y1}	Intermittency sources
P_{y2}	Relaminarization sources
$Re_{\theta c}$	Empirical Reynolds number based on the momentum thickness θ (fluctuations onset)
$Re_{\theta t}$	Empirical Reynolds number based on the momentum thickness θ (transition region onset)
$\widetilde{Re_{\theta t}}$	Transition momentum thickness Reynolds number
Re_L	Reynolds number based on L

S	Invariant measure of the strain rate
S_E	Energy source
S_M	Momentum source
T	Temperature
T_u	Turbulent intensity
T_w	Wall temperature
T_∞	Freestream temperature
U_∞	Freestream velocity (170,1 m/s)
\mathbf{U}	Velocity vector (x,y,z)
U_{fric}	Friction velocity
V_θ	Circumferential velocity component
V_r	Radial velocity component
V_x	Axial velocity component
y^+	Dimensionless distance to wall

Roman lower case letters

a_1	Second SST blending function coefficient
h	Specific static enthalpy
h_{tot}	Specific total enthalpy
k	Turbulent kinetic energy
p'	Modified pressure
q	Wall heat flux
t	Time
y^+	Dimensionless distance to wall

Greek upper case letters

Δs	First mesh cell offset
Ω	Vorticity rate

Greek lower case letters

α	Swirl angle
α_1	k- ϵ model coefficient (5/9)
α_2	k- ω model coefficient (0,44)
α_3	SST model coefficient
β	Yaw angle
β'	k- ω and SST model coefficient (0,09)
β_1	k- ϵ model coefficient (0,075)
β_2	k- ω model coefficient (0,0828)
β_3	SST model coefficient
γ	Intermittency
γ_{eff}	Effective intermittency
γ_{sep}	Modified intermittency to improve separation
δ	Identity matrix
ϵ	Turbulence eddy dissipation rate
λ	Thermal conductivity
μ	Molecular dynamic viscosity of the air (0,000017894 kg/m * s)

μ_{eff}	Effective Viscosity
μ_t	Turbulent viscosity
ρ	Air density ($1,225 \text{ kg/m}^3$)
σ_{k1}	k- ϵ model coefficient (2 in k- ϵ model. 1,176 in SST)
σ_{k2}	k- ω model coefficient (1)
σ_{k3}	SST model coefficient
σ_{w1}	k- ϵ model coefficient (2)
σ_{w2}	k- ω model coefficient (1/0,856)
σ_{w3}	SST model coefficient
τ_{wall}	Wall shear stress
ϕ	SST coefficients
ω	Turbulent frequency (also called specific turbulent dissipation rate)

Operators and scripts

∇	Gradient operator
∇^*	Divergence operator
T	Transposed matrix (superscript)
i, j and k	3 directions of space (subscripts)

1 Background

It is of utmost importance that all the sectors accelerate their transition to sustainability to reach net zero emission target. Decarbonising the aviation industry is a major challenge. To achieve the aim of reducing CO₂ emissions in aviation by 75% by 2050, requires development of ultra-efficient carbon neutral aircrafts (Hydrogen Powered Aviation: A fact-based study of hydrogen technology, 2020). Several disruptive propulsion and electrical technologies needs to be researched and implemented to reach this goal. Liquid hydrogen is one such key enabling sustainable carbon neutral aviation fuel which has a potential to reduce climate impact immensely. The research is going on for implementing direct combustion of hydrogen in the aero gas turbines (although fuel cell technology in aviation for small distance aircrafts is anticipated in future, but there are certain challenges such as the compactness and loss of efficiency at high loads for bigger aircrafts).

Hydrogen has a high gravimetric density which makes it a potential fuel for the future aircrafts, but on the other hand, it has a poor volumetric density which results in penalty of aerodynamic performance, and also increasing the size of the aircraft. Thus liquid hydrogen is kept at cryogenic temperature with proper tank insulation. In an aero gas turbine a viable fuel system heat management system is required to increase the heating value of hydrogen before it reaches the combustor. An effective heat rejection from different location in the gas core can be used to increase the temperature of the hydrogen fuel. The temperature of hydrogen in the fuel line can be increased by different core installed heat exchangers, namely: the precooler, intercooler, and also the turbine-rear-structure outlet guide vanes (TRS-OGV) and the recuperator (Carlos Xisto).

In this work the numerical investigation was done to understand the aerodynamic and aerothermal flow structure on the TRS-OGV.

2 Introduction

In modern aero-engines it is desirable to have high performance which in turn leads to increased bypass ratio and slower rotating fan. There are different effects on the low-pressure expansion system, depending on geared and un-geared turbofans. Thus it is of importance to design the low-pressure expansion system for a wide operational range in terms of swirl, stage loading and gas temperature. The low-pressure expansion system has low pressure turbine (LPT), the turbine rear structure (TRS) and core exhaust nozzle. The TRS is located downstream of the LPT and it has a annular structure with radial struts called Outlet Guide Vanes (OGV). It is a stationary part which has structural purpose of connecting the low pressure shaft bearings with the external rear engine mounts. The OGV also perform aerodynamic function of removing the swirl from the exhaust gas coming from the LPT located upstream. Due to this reason the OGV is mechanically and thermally loaded. The flow over the OGV is complex and thus understanding and validation of heat transfer is crucial for the OGV design.

The project aim is to evaluate heat transfer at the surface of TRS-OGV works to make possible to apply this knowledge on future designs. The goal of this thesis is to contribute to increase the confidence in aerothermal simulations. It was done by performing simulations with a commercial software ANSYS CFX, choosing the turbulence and transition models based on previous studies and comparing those numerical results with experimental data obtained from the Chalmers TRS facility.

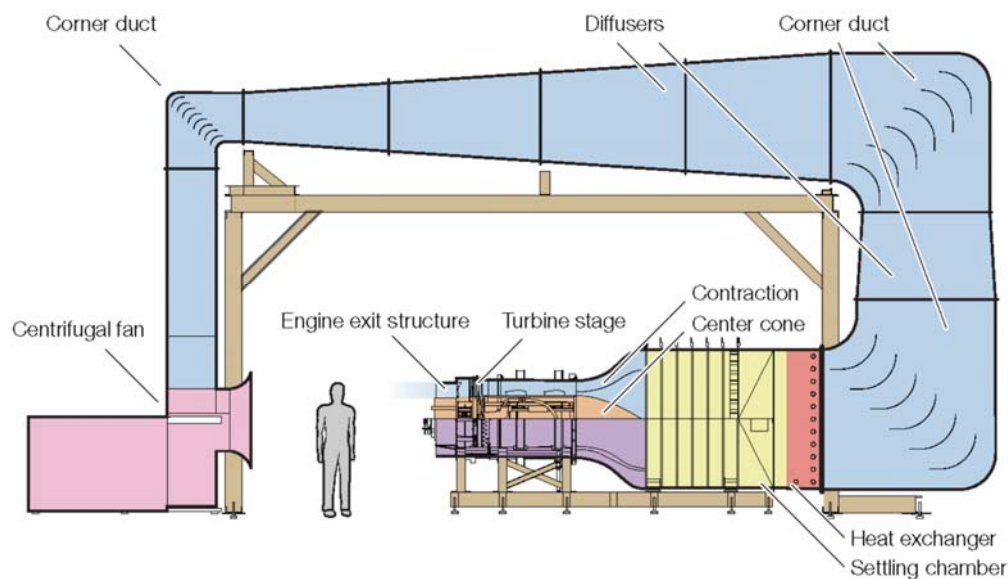


Figure 1. Chalmers OGV-LPT facility (I. Jonsson V. C., 2020)

Numerical simulation tries to be as close to reality as possible, so the Chalmers OGV-LPT facility was imitated. Upstream of the EES there is a turbine, with a stator and a rotor (as can be observed at Figure 4), the stator counts with 72 NGV and the rotor with 60 blades. This is important to point out, because the movement of those 60 blades upstream of the OGV, may be the cause of different phenomena that could occur, like a quickly transition on the boundary layer developed around the 12 OGV blades.

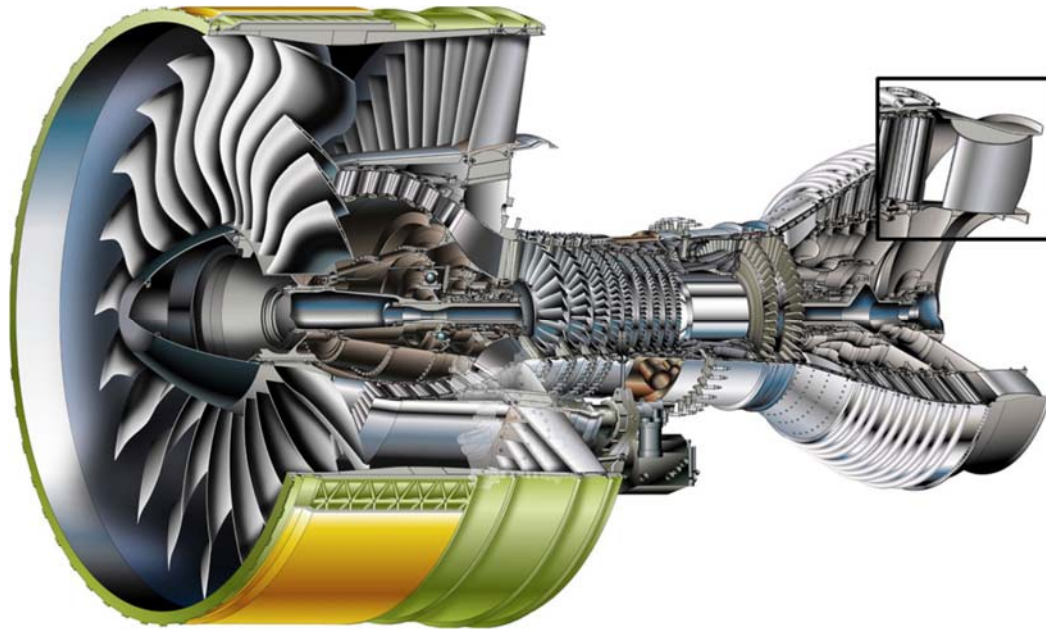


Figure 2. GP7000 turbofan engine, from (B.Rojo, 2017). TRS-OGV highlighted

The OGV can be cooled using the liquid H_2 flowing through the channels inside the OGV and in turn use the heat energy present in the exhaust gas to heat the hydrogen, by conduction, convection and radiation. Due to that, a heat transfer study is vital to understand what it is happening, which are the mechanisms that trigger the transitions, and how to use this information to make more efficient designs, try new layouts and modify operational parameters. That will make possible to make a better use of the heat, reduce the wastage and increase the performance of the whole engine.

When the OGV component are designed numerically, it is necessary to have the experimental data verified. This involves a lot of challenges:

- Due to finite difference approximations the Numerical simulations are bound to have numerical errors. With increasing number of grid points the numerical error decreases but at the cost of computational time (Denton, 2010).
- Experimental data is obtained based on the experimental setup's configurations. The uncertainty errors should be taken into account to reduce the error and offset the data to achieve more accuracy and reliability. B. Rojo analysed these errors on (B.Rojo, 2017).

- Based on the 2 previous concepts, numerical and experimental results will have some discrepancy which can be improved to a certain extent by further increasing the complexity of numerical simulation.
- For the study, several literature was reviewed to understand the experimental and numerical computation. (Chenglong Wang, 2015) studied experimental and numerical study of endwall heat transfer on Outlet guide Vane in a linear cascade. Heat transfer measurements on a linear cascade was done by (B.Rojo, 2017). and the study increased the possibility of further heat transfer study in a new rotating LPT-stage TRS facility. The study on surface roughness effects was discussed on (I. Jonsson V. C., 2018) and (S. Deshpande, 2019). Steady-state heat transfer measurement on the OGV was performed by Jonsson et al. [9]. Initial experimental validation for laminar-turbulent transition in a TRS is discussed in (I. Jonsson S. D., 2020). Furthermore the summarisation of transition from laminar to turbulent boundary layers in turbomachinery flows is discussed in (R.E.Mayle, 1991)
- The present study only account for on-design engine conditions and disregard off-design engine conditions.

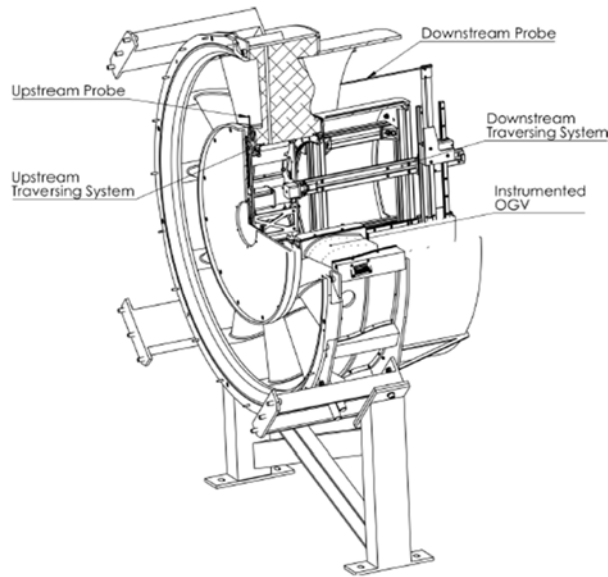


Figure 3. Cross-Section of TRS Source: (B.Rojo, 2017)

3 Theoretical explanations

3.1 OGV airfoil geometry

Further on this report, some terms related to the OGV blade geometry will be used, and those are explained here:

- **Leading edge:** first edge facing the incoming airflow (leftmost point on Figure 4)
- **Trailing edge:** opposite edge to the leading edge
- **Pressure side:** pressure is higher on this side and exert a force towards the blade. The smallest of the surfaces that links both leading and trailing edge (bottom side on Figure 4)
- **Suction side:** pressure is lower, so a suction force is exerted from the blade out. The biggest of the two surfaces (top side)

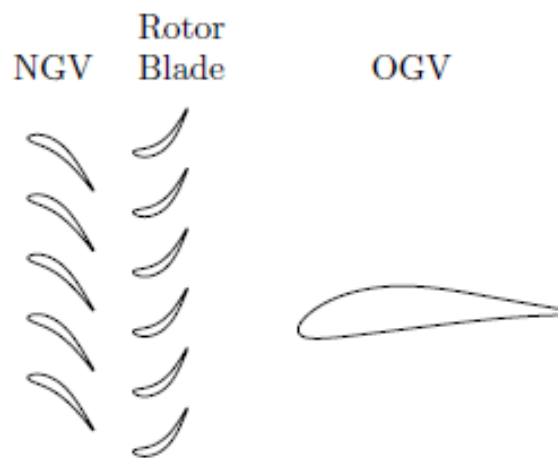


Figure 4. OGV blade shape from (B.Rojo, 2017). Airflow from left to right

3.2 Laminar/transitional/turbulent boundary regions

When there is a flow around an airfoil (OGV Blade), as well as for a flat plate, there is a boundary layer that develops over the wall surface. This boundary region is where the viscous effects are substantial, because of the no slip condition on the fluid-wall interface.

Inside that boundary layer 3 different regions can exist, each of them with different characteristics that affect to the flow behavior, e.g., the heat transfer (the main purpose of this report is to study the heat transfer from the fluid flow to the wall). Those three different regions are (accordingly with (Lienhard, 2020) and (R.E.Mayle, 1991), at a steady state situation):

- **Laminar region:** this region's onset is situated at the leading edge when the fluid flow meets the wall. In this region the viscous forces overcome the turbulent forces. There is no presence of eddies, so the skin friction is low and then, the heat transfer is smaller than in the other two areas.
- **Transitional region:** the length of laminar and transitional regions is similar. As far as it is known, the laminar-turbulent transition could occur in 5 different ways, but all of them agree that the transition is triggered by the production of eddies caused by the transmission of turbulent energy from the freestream flow (assumed turbulent, agreeing with the experimental data). These eddies increase as going away from the leading edge, causing the skin friction to increase, and then, the heat transfer coefficient rises smoothly within the transitional region.
- **Turbulent region:** the turbulent energy inside the boundary layer (that have been mainly transferred from the freestream flow) overcome the viscous forces due to the wall. At this region, the skin friction is higher than at the laminar, so the heat transfer is bigger. For that reason, turbulent regions are sought when designing heat exchangers, because it increases the heat flux.

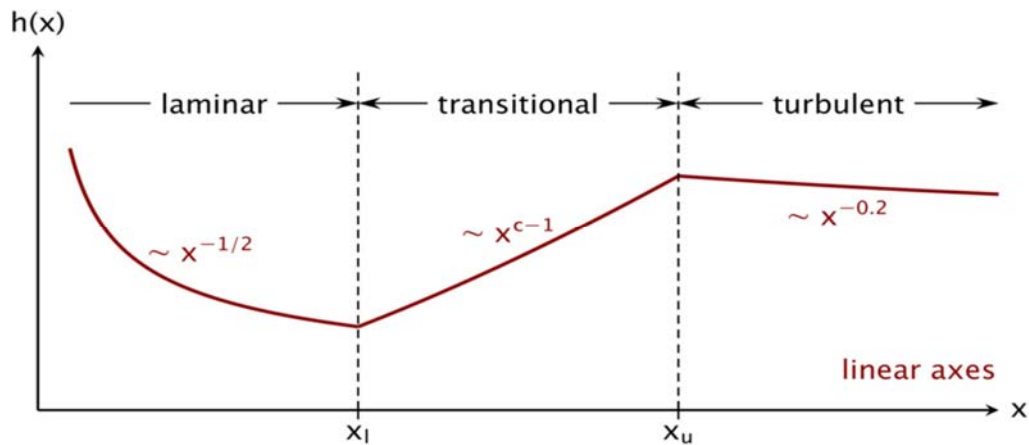


Figure 5. Heat Transfer behaviour in the boundary layer (Lienhard, 2020)

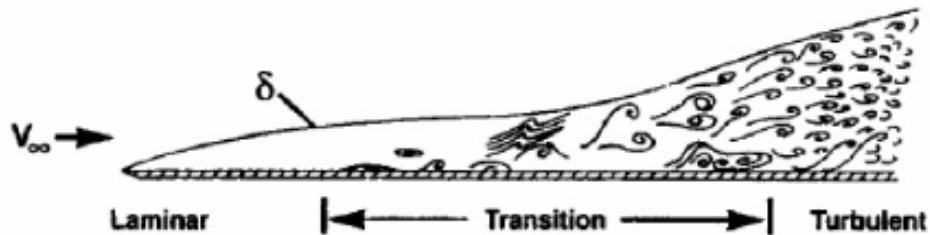


Figure 6. Natural Transition Process (A.A.Torres Sampaio Barros, 2017)

As it was said, there are 5 different modes of transition:

- **Natural Transition:**
 - It starts by the development of 2D instabilities, it amplifies to 3D instabilities which develop eddies, finally the eddies cause a turbulent spot that grow and transform the layer into a turbulent region.
- **By-pass Transition:**
 - The turbulent spot appears directly (without previous instabilities) because of the freestream turbulence.
- **Separated Flow Transition:**
 - Adverse pressure gradients cause the creation of a ‘bubble’. The laminar region gets separated, and when reattach becomes turbulent. On one hand, those ‘bubbles’ can be helpful to force the flow become turbulent quicker than other transition modes. On the other hand, there is not heat transfer to the wall inside the ‘bubble’, so this ‘bubbles’ need a profound study to know which sizes improves the overall heat transfer performance and which worsen it (bigger bubbles will cause losses and should be avoided)
- **Periodic-Unsteady Transition:**
 - It is caused by the wakes from upstream airfoils (NGV and LPT) and may cause the formation of turbulent spots on the laminar layer that cause a fast transition.
- **Reverse Transition:**
 - Also called relaminarization, it means that the turbulent region can suffer a transition to laminar. As the result of large accelerations, the boundary layer is stretched and it leads to a reduction of the turbulent forces, and when viscous forces overcome turbulent, relaminarization occurs.

3.3 Heat transfer coefficient

The aerothermal performance of the TRS is measured by using the HTC, this is a coefficient that account for the rate of heat transfer between solid blade and a fluid flow, expressed in unit per surface area and unit per temperature difference.

$$HTC = \frac{\text{Wall Heat Flux}}{|\text{Wall Temperature} - \text{Freestream Temperature}|} = \frac{q}{T_w - T_\infty} \quad (1)$$

HTC is a way to normalize the heat flux that exist between the wall and the surrounding air. HTC is relevant around the blade surface.

Temperatures were taken from experimental data, inlet and wall blade surface temperatures are known. Inlet is around 15,4°C, so the Freestream Temperature considered has a value of 15,4°C (288,5 K). Blade temperature was set as 31,85 °C.

3.4 Y^+ dimensionless wall distance

Y^+ is a dimensionless quantity that accounts for the distance between the wall and the center of the first mesh cell. The area close to the wall is difficult to simulate properly (get appropriated shear stress values); there are different turbulence and transition models, and each of them treat this area with a different approach.

To be sure that the numerical result is accurate enough, y^+ is fundamental. Ahead there will be an explanation about the models chosen for the numerical simulation, each model requires a different y^+ value. The model selected specifies $y^+ \leq 1$, and the offset for the first cell (this value will be introduced at the simulations at “Mesh”) need to be set to ensure y^+ value.

Based on the flat-plate boundary layer theory, using averaged values, and the following expressions (from (White, 2011)), the offset required was obtained:

$$y^+ = \frac{\Delta s * U_{fric} * \rho}{\mu} \quad (2)$$

$$U_{fric} = \sqrt{\frac{\tau_{wall}}{\rho}} \quad (3)$$

$$\tau_{wall} = \frac{C_f * \rho * U_{\infty}^2}{2} \quad (4)$$

$$C_f = \frac{0.027}{Re_x^{1/7}} \quad (5)$$

$$Re_L = \frac{\rho * U_{\infty} * L}{\mu} \quad (6)$$

Using the values specified at Notations together with Equation 2 to Equation 6, the onset can be obtained:

$$Re_L = \frac{1,225 \frac{kg}{m^3} * 170,1 \frac{m}{s} * 0,2 m}{0,000017894 \frac{kg}{m * s}} = 2\,328\,965,016$$

$$C_f = \frac{0.027}{2\,328\,965,016^{1/7}} = 0,00332$$

$$\tau_{wall} = \frac{0,00332 * 1,225 \frac{kg}{m^3} * 170,1^2 \frac{m^2}{s^2}}{2} = 58,923 \frac{kg}{m * s^2}$$

$$U_{fric} = \sqrt{\frac{58,923 \frac{kg}{m * s^2}}{1,225 \frac{kg}{m^3}}} = 6,935 \frac{m}{s}$$

$$\Delta s = \frac{y^+ * \mu}{U_{fric} * \rho} = \frac{1 * 0,000017894 \frac{kg}{m * s}}{6,935 \frac{m}{s} * 1,225 \frac{kg}{m^3}} = 0,00000211 m$$

$$\boxed{\Delta s = 0,00000211 m = 2,11 * 10^{-6} m}$$

3.5 Turbulent and transitional models

In this section the main mathematical equations used by the solver are presented (get from (ANSYS, 2020)). All the work was perform using Reynolds Averaged Navier-Stokes (RANS) equations.

Not only the equations of the chosen model but the process that was followed to select the model applied. There following models will be introduced and discussed in order to know the advantages and disadvantages of each of them and decide based on all that information:

- $k - \epsilon$ model
- $k - \omega$ model
- SST (Shear Stress Transport) model
- $\theta - \gamma$ Transition model (linked with SST model)

First, regardless of the previous models, there are 2 transport equations that need to be evaluated on all the cells. Here the following expressions are instantaneous equations, to be used by the models they need to be averaged:

$$\frac{\partial \rho}{\partial t} + \nabla * (\rho \mathbf{U}) = 0 \quad (7)$$

$$\frac{\partial(\rho \mathbf{U})}{\partial t} + \nabla * (\rho \mathbf{U} \otimes \mathbf{U}) = -\nabla p + \nabla * \tau + S_M \quad (8)$$

$$\tau = \mu \left(\nabla \mathbf{U} + (\nabla \mathbf{U})^T - \frac{2}{3} \delta \nabla * \mathbf{U} \right) \quad (9)$$

There is a third equation, the energy equation. Total Energy heat transfer model was selected because it accounts for both internal energy and kinetic energy.

$$\frac{\partial(\rho h_{tot})}{\partial t} - \frac{\partial \rho}{\partial t} + \nabla * (\rho \mathbf{U} h_{tot}) = \nabla * (\lambda \nabla T) + \nabla * (\mathbf{U} * \tau) + \mathbf{U} * S_M + S_E \quad (10)$$

$$h_{tot} = h + \frac{1}{2} U^2 \quad (11)$$

Turbulence can be defined as flow fluctuations within time and space (3D), it is usually measured by the Reynolds number that express the relation between the inertial forces and the viscous forces of the flow. A flow is laminar when the viscous forces overcome the inertial forces, leading to low Reynolds numbers. Then, turbulence occurs when inertial forces overcome the viscous forces (due to the no slip walls), giving high Reynolds numbers.

This is a complex problem to be solved. Theoretically, Navier-Stokes's equations can solve both laminar and turbulent flows, but it requires a computing power higher than available right now, so several turbulence (and transitional) models were developed on the last century to allow us to predict the turbulent (and transitional) effects, and some of those models are going to be analyzed on the next pages.

All those models are based on RANS equations, those slightly defer from the instantaneous Navier-Stoke's equations. The flow characteristics can be divided in 2 terms, an average term and a time-varying (fluctuating) term. RANS equations only solve the average term, making possible to solve the problem with the actual computational capacity. Those turbulent models are also known as Statistical, because of this averaging process previously described.

3.5.1 $k - \epsilon$ model

It is an “Eddy Viscosity Turbulence Model”, it means that the physics inside the turbulent problem are explained by the existence of small eddies. Those eddies are created and destroyed unceasingly by the flow.

$k - \epsilon$ is a “Two Equation Turbulence Model”, that kind of models offer a good relation between computational time spent and accuracy. It is called two equations, because it uses two transport equations (together with Continuity, Momentum and Energy

equations) to describe different properties of the turbulence regions. For $k - \epsilon$ model, those two properties are:

- k : Turbulence Kinetic Energy (variance of the velocity's fluctuations).
- ϵ : Turbulence eddy dissipation rate (rate at which velocity's fluctuations dissipates).

Because of adding κ and ϵ terms, some changes need to be done on the previous instantaneous Navier-Stoke equations in order to close the model. These are the 5 transport equations that need to be solved:

- Continuity RANS equation:

$$\frac{\partial \rho}{\partial t} + \frac{\partial}{\partial x_j} (\rho U_j) = 0 \quad (12)$$

- Momentum RANS equation:

$$\frac{\partial (\rho U_i)}{\partial t} + \frac{\partial}{\partial x_j} (\rho U_i U_j) = -\frac{\partial p'}{\partial x_i} + \frac{\partial}{\partial x_j} \left[\mu_{eff} \left(\frac{\partial U_i}{\partial x_j} + \frac{\partial U_j}{\partial x_i} \right) \right] + S_M \quad (13)$$

- Modified pressure:

$$p' = p + \frac{2}{3} \rho k + \frac{2}{3} \mu_{eff} \frac{\partial U_k}{\partial x_k} \quad (14)$$

- Effective viscosity:

$$\mu_{eff} = \mu + \mu_t \quad (15)$$

- Total Energy RANS equation:

$$\begin{aligned} \frac{\partial (\rho h_{tot})}{\partial t} - \frac{\partial \rho}{\partial t} + \frac{\partial}{\partial x_j} (\rho U_j h_{tot}) = \\ \frac{\partial}{\partial x_j} \left(\lambda \frac{\partial T}{\partial x_j} + \frac{\mu_t}{Pr_t} \frac{\partial h}{\partial x_j} \right) + \frac{\partial}{\partial x_j} [U_i (\tau_{ij} - \rho \overline{u_i u_j})] + S_E \end{aligned} \quad (16)$$

- Reynolds stresses equation

$$\rho \overline{u_i u_j} = \mu_t \left(\frac{\partial U_i}{\partial x_j} + \frac{\partial U_j}{\partial x_i} \right) - \frac{2}{3} \delta_{ij} \left(\rho k + \mu_t \frac{\partial U_k}{\partial x_k} \right) \quad (17)$$

- Turbulence Kinetic Energy RANS equation (without buoyancy terms, no buoyancy model):

$$\frac{\partial(\rho k)}{\partial t} + \frac{\partial}{\partial x_j} (\rho U_j k) = \frac{\partial}{\partial x_j} \left[\left(\mu + \frac{\mu_t}{1} \right) \frac{\partial k}{\partial x_j} \right] + P_k - \rho \epsilon \quad (18)$$

- Production rate of turbulence:

$$P_k = \mu_t \left(\frac{\partial U_i}{\partial x_j} + \frac{\partial U_j}{\partial x_i} \right) \frac{\partial U_i}{\partial x_j} - \frac{\partial U_k}{\partial x_k} \left(3\mu_t \frac{\partial U_k}{\partial x_k} + \rho k \right) \quad (19)$$

- Turbulence eddy dissipation rate RANS equation:

$$\frac{\partial(\rho \epsilon)}{\partial t} + \frac{\partial}{\partial x_j} (\rho U_j \epsilon) = \frac{\partial}{\partial x_j} \left[\left(\mu + \frac{\mu_t}{1,3} \right) \frac{\partial \epsilon}{\partial x_j} \right] + \frac{\epsilon}{k} (1,44 P_k - 1,92 \rho \epsilon) \quad (20)$$

There is an extra relation that need to be added to close the equations system, the turbulent viscosity relation to the main turbulent properties of the model (k and ϵ):

$$\mu_t = 0.09 \rho \frac{k^2}{\epsilon} \quad (21)$$

This model, accordingly, to (J.G. Ardila Marín, 2015), give good results on the free flow region, but not close to the walls, at the viscous sublayer. The accuracy is high, but because of the non-linear damping empirical functions, the accuracy is lower than it will be in a model without these. It is a turbulent model, so there are no laminar or transitional regions considered at the boundary layer. This model fails when there's flow separation, i.e., adverse pressure gradients, because of this, is not recommended to turbomachinery applications.

3.5.2 $k - \omega$ model

As the $k - \epsilon$ model, $k - \omega$ is a “Two equations Eddy Viscosity Turbulence Model”. It is like the $k - \epsilon$ model, but ϵ is changed to ω , that is the Turbulent Frequency (also called Specific Turbulent Dissipation Rate) and the values of the constants at the equations are changed too. The Energy, Momentum and Continuity equations still the same as $k - \epsilon$ model. k and ω equations are:

- Turbulence Kinetic Energy RANS equation (without buoyancy terms, no buoyancy model):

$$\frac{\partial(\rho k)}{\partial t} + \frac{\partial}{\partial x_j}(\rho U_j k) = \frac{\partial}{\partial x_j} \left[\left(\mu + \frac{\mu_t}{2} \right) \frac{\partial k}{\partial x_j} \right] + P_k - 0,09 \rho k \omega \quad (22)$$

- Turbulence Frequency RANS equation (without buoyancy terms, no buoyancy model):

$$\frac{\partial(\rho \omega)}{\partial t} + \frac{\partial}{\partial x_j}(\rho U_j \omega) = \frac{\partial}{\partial x_j} \left[\left(\mu + \frac{\mu_t}{2} \right) \frac{\partial \omega}{\partial x_j} \right] + \frac{5}{9} \frac{\omega}{k} P_k - 0,075 \rho \omega^2 \quad (23)$$

The extra equation for the turbulent viscosity for this model is:

$$\mu_t = \rho \frac{k}{\omega} \quad (24)$$

This model, accordingly, to (J.G. Ardila Marín, 2015), give good results close to the walls on the viscous sublayer, but not on the free flow region. The accuracy is higher than $k - \epsilon$ model, because of the lack of damping empirical functions. Another problem is the sensitivity to freestream conditions, different initial values will cause different results, it is a huge drawback for the accuracy. It is a turbulent model, so there are no laminar or transitional regions considered at the boundary layer. This model fails when there's flow separation, i.e., adverse pressure gradients, because of this, is not recommended to turbomachinery applications.

3.5.3 SST (Shear Stress Transport) model

As can be observed from both $k - \epsilon$ and $k - \omega$ model, there is one solution that seems obvious, as long as the $k - \epsilon$ model works properly on the free flow region and the $k - \omega$ model works well closed to the wall, a mix between both models will have a good accuracy ewhere. This model is the SST model, is a model that have a blending function (F_1) that change between the two original models based on the distance to the nearest surface, it is done with an 'extra' term that accounts for the difference between ω and ϵ equations.

There is a second blending function that acts as a viscosity limiter, because previous models (BSL model) had problems with overprediction of the viscosity. The coefficients (ϕ_3) use at the following expressions are a linear combination of the corresponding coefficients of both $k - \epsilon$ (ϕ_1) and $k - \omega$ (ϕ_2) models (except for $\alpha_{k1} = 1,176$), based on the first blending function (F_1):

$$\phi_3 = F_1 * \phi_1 + (1 - F_1) * \phi_2 \quad (25)$$

There are only 4 cases:

$$\alpha_3 = F_1 * \frac{5}{9} + (1 - F_1) * 0,44$$

$$\beta_3 = F_1 * 0,075 + (1 - F_1) * 0,0828$$

$$\alpha_{k3} = F_1 * 1,176 + (1 - F_1) * 1$$

$$\alpha_{\omega 3} = F_1 * 2 + (1 - F_1) * \frac{1}{0,856}$$

F_1 is a complex hyperbolic tangent function that depends on the distance to closest wall. k and ω equations are rewritten as:

- Turbulence Kinetic Energy RANS equation (without buoyancy terms, no buoyancy model)

$$\frac{\partial(\rho k)}{\partial t} + \frac{\partial}{\partial x_j}(\rho U_j k) = \frac{\partial}{\partial x_j} \left[\left(\mu + \frac{\mu_t}{\sigma_{k3}} \right) \frac{\partial k}{\partial x_j} \right] + P_k - 0,09 \rho k \omega \quad (26)$$

- Turbulence Frequency RANS equation (without buoyancy terms, no buoyancy model)

$$\begin{aligned} & \frac{\partial(\rho \omega)}{\partial t} + \frac{\partial}{\partial x_j}(\rho U_j \omega) = \\ & \frac{\partial}{\partial x_j} \left[\left(\mu + \frac{\mu_t}{\sigma_{\omega 3}} \right) \frac{\partial \omega}{\partial x_j} \right] + (1 - F_1) 2 \rho \frac{1}{\frac{1}{0,856} \omega} \frac{\partial k}{\partial x_j} \frac{\partial \omega}{\partial x_j} + \alpha_3 \frac{\omega}{k} P_k - \beta_3 \rho \omega^2 \end{aligned} \quad (27)$$

The extra equation for the turbulent viscosity for this model is:

$$\mu_t = \frac{a_1 \rho k}{\max(a_1 \omega, S F_2)} \quad (28)$$

S is a measure of the strain rate and a_1 is a coefficient that will not have any influence in the result as long as the viscosity does not drop really low.

This model, accordingly, to (J.G. Ardila Marín, 2015), give more realistic results than the two previous models, but there are room for improvement, because the model assume the boundary layer close to the wall as turbulent, but there are a laminar and a transitional section that needs to be take into account (in our model the laminar region cannot be disregard).

3.5.4 $\theta - \gamma$ Transition model (linked with SST model)

There are several reports that validate the application of Langtry-Menter $\theta - \gamma$ transition model together with SST $k - \omega$ model, e.g. (A.A.Torres Sampaio Barros, 2017). This model has developed with the following limitations:

- Works with a correlation for by-pass transition, but separation transition can be predicted too.
- Only works when there is a defined freestream region (like airfoils)
- Buoyancy forces cannot be considered
- Wall cannot move
- $y^+ \leq 1$

All these limitations match perfectly with the current study.

3.5.4.1 Transition theory

This model is a “Four Equations” model, the first 2 equations are k and ω equations from SST model (with some changes) and the other 2 equations are:

- γ : Intermittency (% of time that turbulent fluctuations are present on each cell)
- $\widetilde{Re}_{\theta t}$: Transition Momentum Thickness Reynolds number

Transition Momentum Thickness Reynolds Number is a Reynolds number calculated using Momentum thickness. Momentum Thickness (θ), is a theoretical distance that account for the viscous effects close to the airfoil. It is related to the drag force over the blade, that can be related to a momentum defect due to the presence of the wall and the formation of the boundary layer. It is used to measure the boundary layer thickness.

At Figure 7, boundary layer thickness δ can be observed. At the fully turbulent boundary layer region, the velocity profile outside the boundary layer is constant and agrees with the freestream velocity. Inside it follows a parabolic distribution.

As can be observed at Figure 7, momentum thickness is the distance that the airfoil surface needs to be displaced away, to have under the ‘new’ surface position the same velocity profile area, than the area that is lacking over the surface if a constant velocity profile was searched. It can be defined too as the thickness of an ‘empty’ layer placed in between the surface and a constant freestream velocity profile.

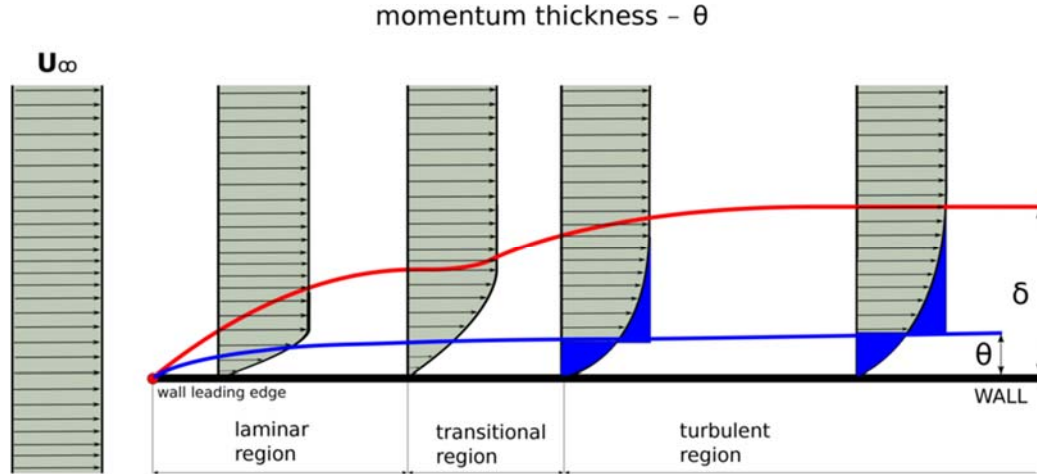


Figure 7, Momentum Thickness Explanation (CFDSupport, s.f.)

Now, there are three more parameters to mention before starting with the equations:

- Re_{θ_t} is the Reynolds Number based on the momentum thickness θ , so it can be translated as a position over the wall (starting at the leading edge). This number describe the position where transition occur (change from laminar to transition)
- Re_{θ_c} it accounts for the position where the fluctuations that lead to turbulence (intermittency) start to increase (slightly before than Re_{θ_t})
- F_{length} is the length of the transitional region.

Those three values are defined with empirical expression got from experimental data. $\widetilde{Re_{\theta_t}}$ is an expression that is calculated ewhere and when it matches with Re_{θ_t} and Re_{θ_c} changes are done in order to start the transition region. Re_{θ_c} and F_{length} empirical functions depend on $\widetilde{Re_{\theta_t}}$.

$$\begin{aligned} Re_{\theta_t} &= f(Tu, \lambda_{\theta}) \\ F_{length} &= f(\widetilde{Re_{\theta_t}}) \\ Re_{\theta_c} &= f(\widetilde{Re_{\theta_t}}) \end{aligned}$$

3.5.4.2 Transition onset

Capture the transition onset is one of the primal targets of this project, and here the principal characteristics and limitations are going to be explained.

As explained before, there is a transitional region on the boundary layer developed around the blade. This boundary layer is a key feature when speaking about heat transfer or turbulent energy transport. The transition region start when the turbulent energy inside the layer reach a particular level calculated by correlations. That location is the one that want to be captured as accurately as possible.

The transition onset location is triggered by three parameters (based on (R.E.Mayle, 1991)):

- Turbulent intensity outside the boundary layer
- Thickness momentum Reynold number
- Acceleration parameter

The same that happens for the heat transfer modelling occurs for this factor. Because of time limitations, the latter 2 parameters were not thoroughly analyzed, only turbulent intensity was deeply studied. The other two are fields suggested to further analysis in future projects.

3.5.4.3 Transport equations

Now, the equations that integrate the transitional part of the model are presented:

- Intermittency RANS equation:

$$\frac{\partial(\rho \gamma)}{\partial t} + \frac{\partial}{\partial x_j} (\rho U_j \gamma) = \frac{\partial}{\partial x_j} \left[\left(\mu + \frac{\mu_t}{1} \right) \frac{\partial \gamma}{\partial x_j} \right] + P_{y1} - E_{y1} + P_{y2} - E_{y2} \quad (29)$$

- Intermittency sources:

$$P_{y1} = 2 F_{length} \rho S [\gamma F_{onset}]^{0.5} \quad (30)$$

- Intermittency sinks:

$$E_{y1} = \gamma P_{y1} \quad (31)$$

- Functions to switch intermittency production:

$$F_{onset} = \max(F_{onset2} - F_{onset3}, 0) \quad (32)$$

$$F_{onset3} = \max \left(1 - \left(\frac{\rho k}{2.5 \mu \omega} \right)^3, 0 \right) \quad (33)$$

$$F_{onset2} = \min(\max(F_{onset1}, F_{onset1}^4), 2) \quad (34)$$

$$F_{onset1} = \frac{\rho \gamma^2 S}{2,193 \mu Re_{\theta c}} \quad (35)$$

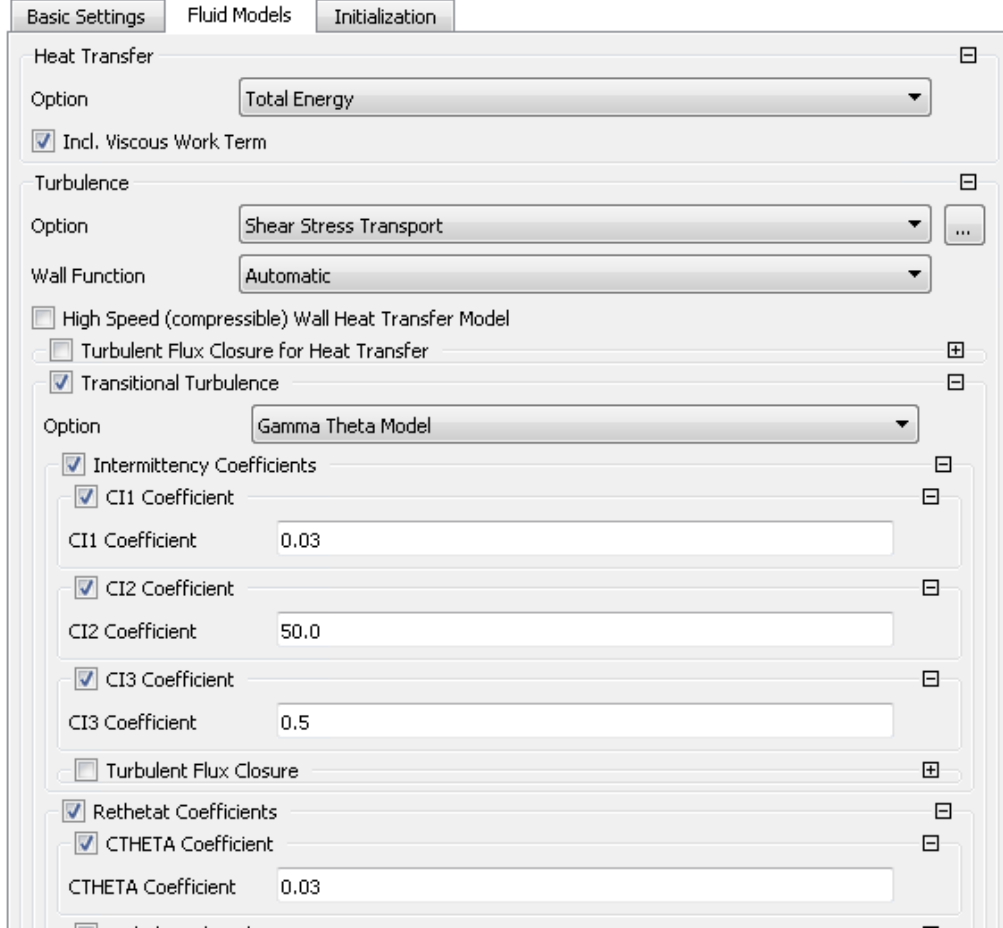


Figure 8. Coefficients gamma theta equations (for P_{y1} , P_{y2} and E_{y2} equations)

- Relaminarization (this model allow the boundary layer turbulent flow to become laminar again):
 - Relaminarization sources:

$$P_{y2} = 2 * 0,03 \rho \Omega \gamma \left[e^{-\left(\frac{\rho k}{4 \mu \omega}\right)^4} \right] \quad (36)$$

- Relaminarization sinks:

$$E_{y2} = 50 \gamma P_{y2} \quad (37)$$

- Transition Momentum Thickness Reynolds number RANS equation

$$\frac{\partial(\rho \widetilde{Re_{\theta t}})}{\partial t} + \frac{\partial}{\partial x_j} (\rho U_j \widetilde{Re_{\theta t}}) = P_{\theta t} + \frac{\partial}{\partial x_j} \left[\left(2 (\mu + \mu_t) \frac{\partial \widetilde{Re_{\theta t}}}{\partial x_j} \right) \right] \quad (38)$$

- Theta sources:

$$P_{\theta t} = 0,03 \frac{\rho^2 U^2}{500 \mu} (Re_{\theta t} - \widetilde{Re_{\theta t}}) (1 - F_{\theta t}) \quad (39)$$

- Blending function $F_{\theta t}$ use to override convection and diffusion empirical values at the freestream using Equation 39:

$$F_{\theta t} = \min \left(\max \left(e^{-\left(\frac{\rho \omega \gamma^2}{\mu 1 \cdot 10^5} \right)^2} e^{-\left(\frac{\frac{\gamma}{375 \Omega \gamma \widetilde{Re_{\theta t}} \mu}}{U^2 \rho} \right)^4}, 1 - \left(\frac{\gamma - 0,02}{0,98} \right)^2 \right), 1 \right) \quad (40)$$

There are some changes that needs to be done on the two turbulent equations (k and ω) respect to the SST model:

- Turbulence Kinetic Energy RANS equation:

$$\frac{\partial(\rho k)}{\partial t} + \frac{\partial}{\partial x_j} (\rho U_j k) = \frac{\partial}{\partial x_j} \left[\left(\mu + \frac{\mu_t}{\sigma_{k3}} \right) \frac{\partial k}{\partial x_j} \right] + \widetilde{P}_k - \widetilde{D}_k \quad (41)$$

- Modified Turbulence Production Term due to Viscous Forces:

$$\widetilde{P}_k = \gamma_{eff} P_k \quad (42)$$

- Old Turbulent Production Term due to Viscous Forces:

$$P_k = \mu_t \left(\frac{\partial U_i}{\partial x_j} + \frac{\partial U_j}{\partial x_i} \right) \frac{\partial U_i}{\partial x_j} - \frac{2}{3} \frac{\partial U_k}{\partial x_k} \left(3 \mu_t \frac{\partial U_k}{\partial x_k} + \rho k \right) \quad (43)$$

- Modified Intermittency equations to improve Separation prediction:

$$\gamma_{eff} = \max(\gamma, \gamma_{sep})$$

$$\gamma_{sep} = F_{\theta t} \left[\min \left(2 e^{-\left(\frac{\rho k}{20 \mu \omega}\right)^4} \max \left[\left(\frac{\rho \gamma^2 S}{3,235 \mu Re_{\theta c}} \right) - 1, 0 \right], 2 \right) \right] \quad (44)$$

$$\tilde{D}_k = \min \left(\max \left(\gamma_{eff}, \frac{1}{10} \right), 1 \right) 0,09 \rho k \omega \quad (45)$$

- Turbulence Frequency RANS equation:

$$\begin{aligned} & \frac{\partial(\rho \omega)}{\partial t} + \frac{\partial}{\partial x_j} (\rho U_j \omega) = \\ & \frac{\partial}{\partial x_j} \left[\left(\mu + \frac{\mu_t}{\sigma_{\omega 3}} \right) \frac{\partial \omega}{\partial x_j} \right] + (1 - \tilde{F}_1) 2 \rho \frac{1}{\frac{1}{0,856} \omega} \frac{\partial k}{\partial x_j} \frac{\partial \omega}{\partial x_j} + \alpha_3 \frac{\omega}{k} P_k - \beta_3 \rho \omega^2 \end{aligned} \quad (46)$$

Some failures were noticed when using SST turbulent model, in some cases the blending function failed close to the wall choosing k- ϵ model instead of k- ω . Those problems were solved by the mean of the new blending function \tilde{F}_1 (F_1 is the same complex hyperbolic tangent function from the SST turbulent model):

$$\tilde{F}_1 = \max \left(F_1, e^{-\left(\frac{\rho \gamma \sqrt{k}}{120 \mu}\right)^8} \right) \quad (47)$$

This model has a better performance than the SST turbulent model at the turbulent equations because of the new \tilde{F}_1 blending function that avoid potential problems. It also adds 2 new equations that allow the designer to better define the boundary layer. For the 3 previous models, the boundary layer was assumed as turbulent all over the airfoil surface, now laminar and transitional regions are accounted. The modes of transition that the model is design to predict accurately are separation and by-pass transition modes, the two modes that are expected to exist over the airfoil, accordingly with (I. Jonsson S. D., 2020).

3.6 Heat transfer modelling

The experimental setup is based on a water core with a isolated shell. In (Dhanasegaran, 2018), heat transfer on the OGV is investigated experimentally. In (Dhanasegaran, 2018), to understand the conjugate heat, resolving of two fluid domains with a solid intermediate body has been discussed. The built-in functions in CFX to investigate heat transfer coefficient either by constant blade surface temperature or constant heat flux was used to simplify the numerical simulations. It should be noted that these assumption does not describe the heat transfer process in a conjugate system accurately.

To evaluate the influence of these two assumptions the heat transfer of a flat plate at conditions corresponding to the condition at suction side of the OGV at midspan was investigated based on experimental correlations given below.

$$Nu_x = 0.332Pr^{\frac{1}{3}}Re_x^{\frac{1}{2}} \quad (48)$$

$$\text{when } T_w = \text{const}, Re_x < 5 * 10^5, 0.6 < Pr < 50$$

$$Nu_x = 0.453Pr^{\frac{1}{3}}Re_x^{\frac{1}{2}} \quad (49)$$

$$\text{when } q_w = \text{const}, Re_x < 5 * 10^5, 0.6 < Pr < 50$$

Two different cases were run, with two different simplifications used:

- Constant blade surface temperature (305 K)
- Constant heat flux through blade surface $\left(550 \frac{W}{m^2}\right)$

Based on Figure 9, laminar regions, transition length and transition onset are not matching. On the other hand, fully developed turbulent region is the same for both cases.

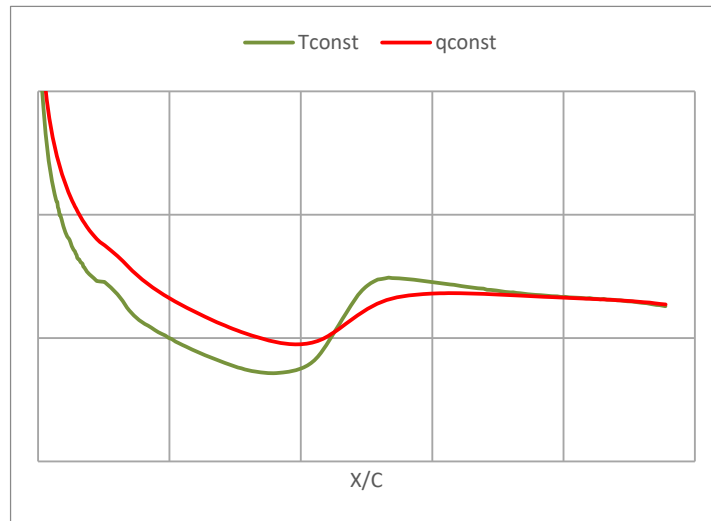


Figure 9. Comparison of expected results for the 2 simplifications

4 Methodology

On this section the main objective is to explain how the data was obtained:

- Introduction to the experimental setup and devices used for the gathering of the experimental data (with further information on the references, (I. Jonsson V. C., 2020), (B.Rojo, 2017), (I. Jonsson S. D., 2020) and (I.Jonsson, 2020))
- Summary about how the interpolation of the experimental data was carried out and what is necessary to validate this interpolated data
- Numerical simulations set up

4.1 Experimental data

The experimental data was obtained from the Chalmers OGV-LPT test facility, that had the following instrumentation (referred to Figure 10):

- One multi-hole probe (5-probe) upstream the OGV blade, at the “Inlet” plane.
- One multi-hole (7-probe) downstream the OGV blade, at the “Evaluation Plane”.
- One Pitot probe for setting a pressure reference for data normalization (P-ref).
- Pressure taps distributed over the surface of the blade (black dots)

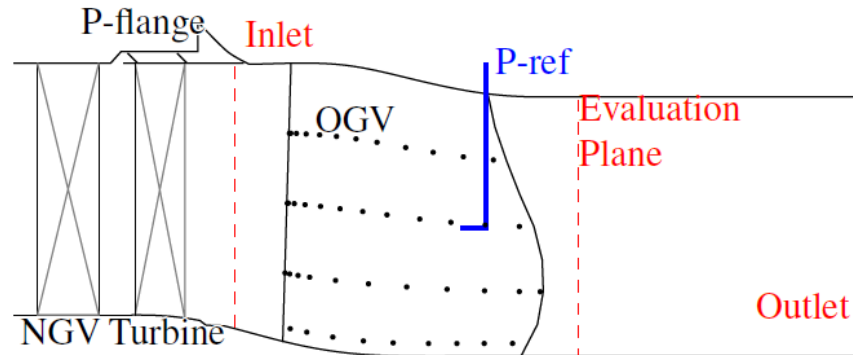


Figure 10. Location of pressure taps, reference probe and evaluation planes

Multi-holes probes are devices with multiple holes in their tips (5 and 7 at Chalmers facility) that are positioned against the incoming flow (5-holes turned 16° degrees and 7-holes straight). There is an angle between the airflow direction and the multi-hole probe orientation and due to this angle, the different holes will capture dissimilar pressure values and based on those differences, it is possible to calculate:

- Total Pressure and Static Pressure
- 3 Velocity components (axial, radial and circumferential)
- Air Density
- Temperature

➤ Swirl and Yaw angle

The Pitot probe is a device that can measure both static and total pressure, and those values, combined with the information got from the multi holes probes, can be used to obtain pressure coefficients. So, the parameters that can be calculated are:

$$C_{p_0} = \frac{P_t - P_{t,Pitot}}{P_{t,Pitot} - P_{s,Pitot}} \quad (50)$$

$$C_p = \frac{P_s - P_{t,Pitot}}{P_{t,Pitot} - P_{s,Pitot}} \quad (51)$$

Pitot probe, as well as multi holes probes were placed on 1000 different places equally distributed circumferentially and radial at the Inlet plane (and 1000 places at the evaluation plane).

77 pressure taps were distributed all over the blade surface (at 75%, 50%, 25% and 12,5% span) which target is to measure the static pressure. Those measures are possible because the blade was specially manufactured (stereolithography) with channels inside to make the measurements possible. Pitot probe was also placed at those 77 spots to get both total and static pressure; with all those data is possible to get the static pressure coefficient.

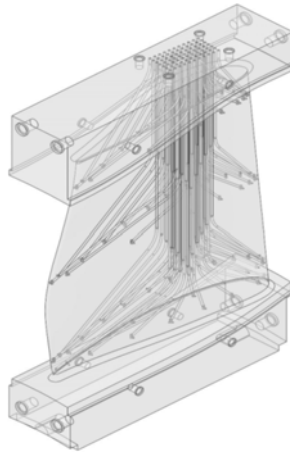


Figure 11. OGV blade with 77 pressure taps and channels (B.Rojo, 2017)

InfraRed Thermography technology was used to obtain experimental heat flux data over the OGV blade. These measurements were designed and performed by Jonsson et al. (I. Jonsson V. C., 2020), they obtained the heat transfer coefficient distribution over an OGV blade at the Chalmers rig, trying to reduce the uncertainties to the minimum and using a problem formulation that accounted for the three known heat transfer methods: conduction, convection, and radiation.

4.2 Processing of experimental data

To validate the experimental data obtained, a simulation with a commercial software (ANSYS) needs to be done, and both data should match. The simulations need some input data to be used as boundary layer. During experiments several quantities were measured over the inlet plane surface, and based on that data, the following features were used:

- Total Pressure at the Inlet plane (Figure 10)
- Temperature at Inlet
- Velocity components (cartesian) at Inlet

Total pressure, temperature and velocity components are available from experimental data at inlet, however near endwalls (hub and shroud) there is no data because probing these areas is not possible, therefore, the experimental data could not be used one to one or directly as inlet into the numerical domain. Data has to be pre-processed before it could be used as inlet and it was done by extrapolating the nearest neighbour and then interpolating into the numerical mesh.

Two grids are available, one show the distribution of the experimental measurements and has data values assigned to each point (pressure, velocity ...); the other grid has no data (only coordinates), was exported from ANSYS TurboGrid and correspond to the geometry created over the virtual space. The experimental grid is slightly smaller than the virtual grid (because of experimental limitations), this problem was solved as follows:

- Virtual grid coordinates were modified to get that both grids were centered around the same point and following the same axis.
- An interpolation of the experimental data into the virtual mesh needs to be done. A interpolation requires a data grid (experimental) bigger than the turbomesh grid (virtual), to get this, the most external rows and columns were copied and pasted away, keeping the distance pattern used on the experimental.
- Interpolation was done from the data on the 'extended' experimental grid, to the virtual grid

In Figure 12 and Figure 13, it can be observed that the extended experimental grid (blue), is bigger than the virtual grid (orange), so interpolation is possible. The last row close to the hub and the last close to shroud, as well as the rightmost and leftmost columns (blue grid) have exactly the same values as their correspondingly immediately inner point. Extended points can be observed at Figure 12 inside boxes.

A linear interpolation was done, it means that between two adjacent points of the original grid, a 'line' is created, and all the points from the digital grid that are in between, are given a value accordingly to this 'linear' approach; this is only a 1D simplification, the real interpolation was 2D (3D is not necessary, because the data was get from planes, only 2 coordinates vary from point to point).

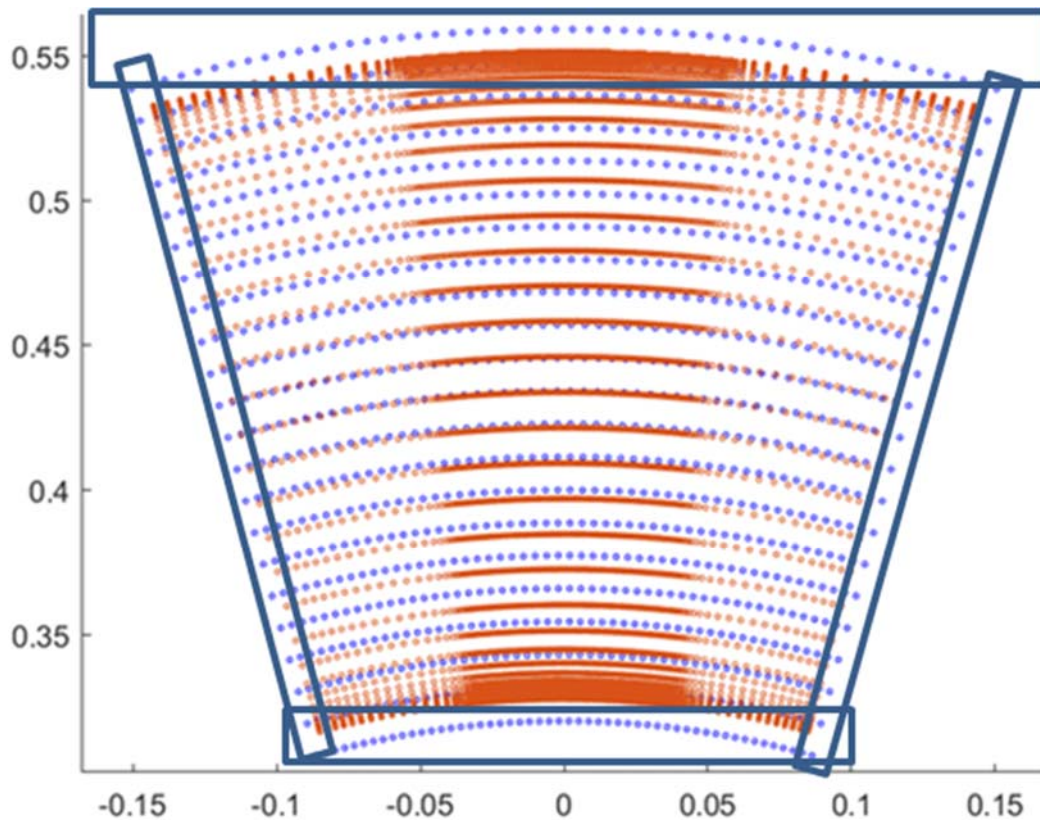


Figure 12. Extended Experimental Grid (blue) vs Virtual Grid (orange) Inlet Plane

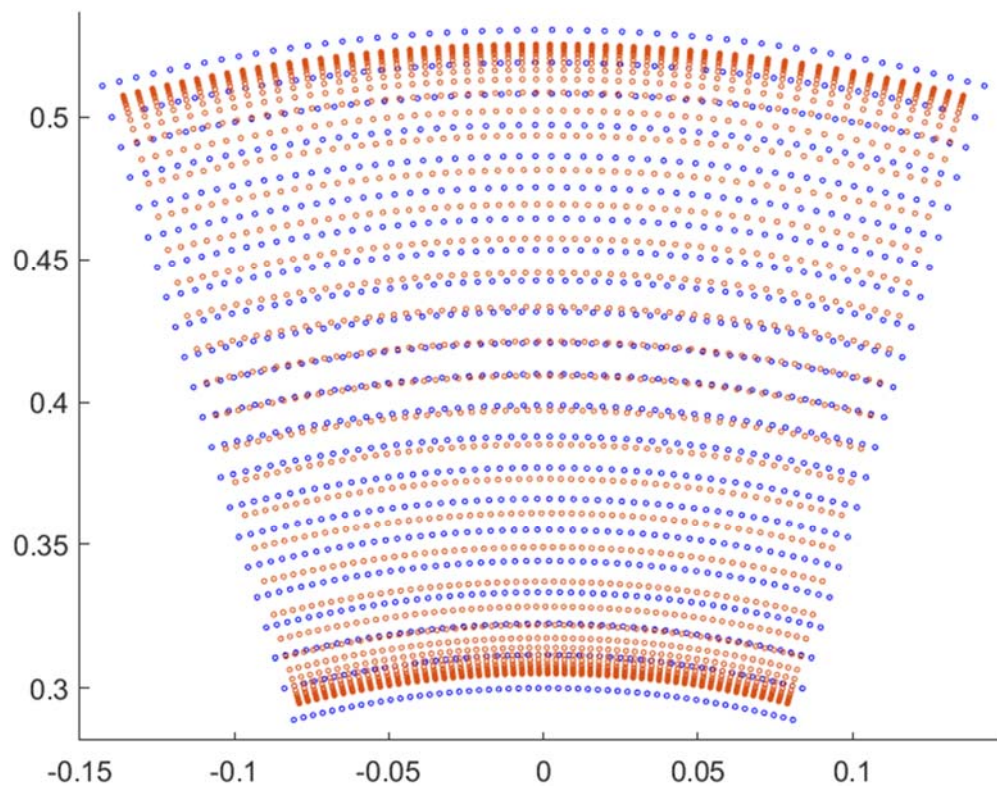


Figure 13. Extended Experimental Grid (blue) vs Virtual Grid (orange) Eval. Plane

Two interpolations were carried out, one for the Inlet plane and the other one for the Evaluation Plane. The processing of experimental data to fit the domain was done using Matlab.

It can be observed at Figure 13 that the Virtual Grid is finer close to the trailing edge of the blade, with the only aim of getting more accurate results where the variations are high (close to the walls). The same happens close to both hub and shroud (Figure 12 and Figure 13).

4.3 Numerical simulations

Here in the implementation of the numerical instrumentation there are five steps. First Simulation's set up process has 5 pronounced steps:

1. Geometry
2. Mesh
3. Numerics: boundaries, models, input data ...
4. Running and Mesh Independence Study
5. Post-Processing (Results)

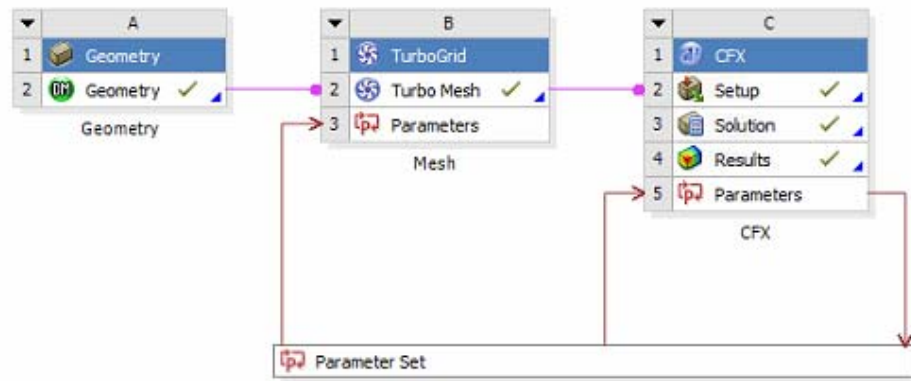


Figure 14. Ansys Workbench layout

4.3.1 Geometry

The first step, when starting is to obtain a 3D TRS-OGV model. The goal is to get a 'geometry' on which meshing is possible.

Previous studies were done over TRS-OGV on Ansys by the Chalmers Department of Mechanics and Maritime Sciences, so there were CAD files available. Those files were used by previous researchers, so the accuracy was granted.

Ansys has two different geometry editors: SpaceClaim and DesignModeler. The latter was chosen because one of its characteristics is the use of the same "geometry modeling

kernel (software)” than SolidWorks; e single CAD file available was produced with SolidWorks, so the choice was pretty easy.

At Figure 15 the geometry result over DesignModeler can be observed. The planes introduced at Figure 10 can be seen, from the left to the right: inlet, blade, experimental plane and outlet. There are some changes that need to be done over this geometry to make it suitable for the data get from the interpolation, but they will be done at the meshing step. The main objective was to export points to define as well as possible the blade surface, and it was done satisfactorily.

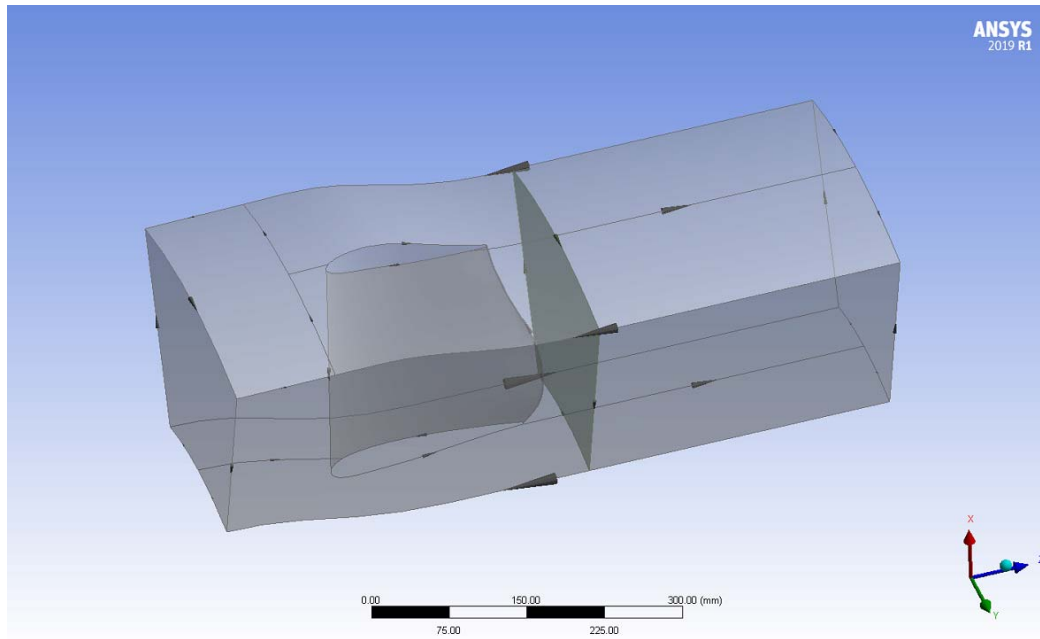


Figure 15. TRS-OGV on Design Modeler

4.3.2 Mesh

TurboGrid was selected for meshing. On challenging area when implementing numerical meshes is to place inlet and evaluation planes at their correct positions. The experimental data was measured at specific distances upstream and downstream the leading and the trailing edges correspondingly.

In Figure 16 an reduced domain can be observed (compared to the extended domain on Figure 10). This reduced domain was used to reduce computational time when checking particular features. Results presented later (e.g., blade loading, outlet contours ...) were obtained from the extended domain.

The simulation was done over 1 OGV blade, the real model has 12 blades (see Figure 3), but because of symmetry, the results over 1 blade can be extended to the rest of the blades. That is why 2 planes with a symmetry role are needed (see Figure 17).

Following the explanation at “Y+ dimensionless wall distance”, the offset value was set as $2,11 * 10^{-6}m$. The last parameter to be set on TurboGrid is the global size factor a parameter that increase or decrease the number of elements of the grid, it was extremely useful for the mesh independence study that was done. A value close to 1 is a good guess to start, now it does not really matter, because this value will be changed several times while carrying out the mesh independence study. Meshing was done by default with an H-grid mesh type.

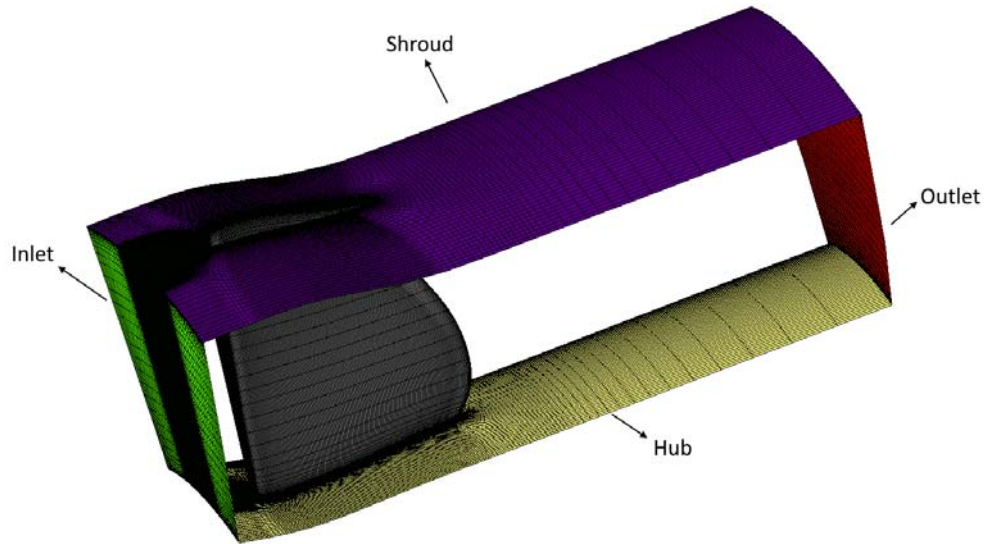


Figure 16. Domain Mesh

At Figure 16 meshing results and different layers created can be observed. The grey layer in the middle corresponds the blade; the green layer is the inlet and the red one is the outlet (evaluation plane); purple correspond to the shroud and orange to the hub. There are 2 more layers that were suppressed at Figure 16 but can be seen at Figure 17; those 2 layers complete the ‘cube’ that surrounds the blade and are called ‘periodic’, those surfaces do not correspond to a physical element (as inlet and outlet planes), are used to close the domain, and had a symmetric role.

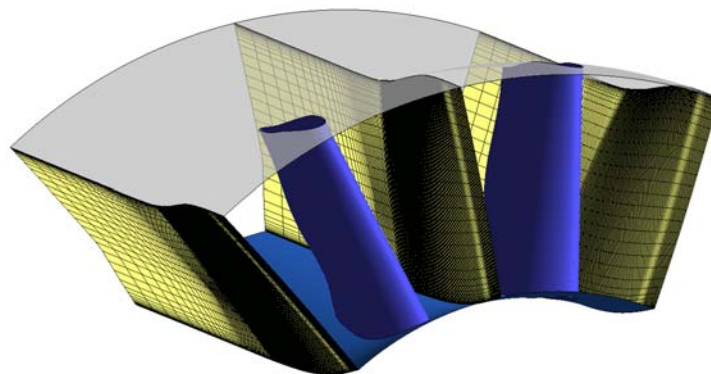


Figure 17. Symmetry planes at 2 blades domain

4.3.3 Numerical setup

This is probably the most influential step, because there are a lot of different parameters to be set, with several options for each one and all of them have a direct impact on the results.

The mesh obtained on the previous step was imported to the new tool, CFX-Pre. Simulations could have been handled with either CFX or Fluent. CFX was chosen because it is recommended for turbomachinery applications, by the way, both software could have been used for this task. The following topics need to be discussed:

- Boundary conditions
- Inlet and outlet conditions from experimental data
- Analysis type
- Turbulence and transitional model

4.3.3.1 Boundary conditions

Boundary conditions need to be set for the 6 different surfaces that was meshed (inlet, outlet, hub, shroud, blade and ‘periodic’).

Hub, shroud, and blade are real surfaces, so they are defined as ‘no slip walls’, with ‘smooth roughness’ (brand new pieces) and the heat transfer through the wall is set to ‘adiabatic’ for hub and shroud. The blade boundary conditions was done in set according to constant surface temperature and constant heat flux, see Section 3.6.

Inlet and outlet are not real physical surfaces whose main purpose is to set the pressure, temperature and velocity values got from the experiment. It will be explained on the next section.

Both ‘periodic’ planes are set as ‘Interface’, so the solver will know that there is a symmetry condition over those planes and can simulate the flow properly. Those planes did not correspond to a physical element.

4.3.3.2 Inlet and Outlet initial conditions

At the previous section, it was said that Inlet and Outlet planes are used for setting pressure, temperature, and velocities contours. There are 3 different possibilities when setting these inflow/outflow boundary conditions, one was choose based on the experimental data. The following data profiles are needed:

- Total Pressure at the Inlet plane
- Temperature at the Inlet plane
- Flow direction components (velocity) at the Inlet plane
- Static pressure at the Outlet plane

As explained before, this data is available from the experimental results got at the Chalmers rig. These data were linearly interpolated over the inlet and outlet planes built on Ansys workspace from the experimental grid by using Matlab. These inlet and outlet contours were imported into CFX-Pre and applied to the analogous planes.

At both planes the flow need to be set as subsonic or supersonic. The Mach number (M) from the experiment is under 0,9 at the whole TRS domain, so the flow is ‘incompressible’ ($M < 1$), i.e., subsonic.

There is a LPT section upstream of inlet OGV plane, so the characteristics of that LPT will influence the turbulent properties. To capture the turbulent characteristics there are few options that can be selected, and each option set different parameters. The one selected ask for:

- **Turbulent intensity:** accordingly to the experiments, the value is around 4,6%. Three different simulations were done, 4%, 5% and 6% (based on experimental measurements (I. Jonsson V. C., 2018) and (I. Jonsson S. D., 2020)). This values will affect the turbulent levels downstream, as well as onset transition, HTC
- **Eddy length scale:** it was assumed as 50% of the pitch from the previous LPT blade (1 cm), but different values were tried too: 1,5 cm, 0,8 cm, 0,5 cm, 0,37 cm and 0,1 cm.

4.3.3.3 Analysis type

The experimental data was averaged to be able to assume steady-state conditions, so the simulations should be carried out following the accordingly steady-state model. TRS-OGV is a fixed element of the engine, it is not rotating, then, the motion of the system was established as ‘stationary’.

The reference pressure needs to be set too, typical values are 0 atm and 1 atm; 0 atm was not selected because it may cause issues when, so all the contours that will be showed further on this report will be based on a 1 atm reference pressure.

The domain is defined as ‘fluid’ and the fluid as ‘air ideal gas’, symmetries stated as fluid-fluid boundaries. Combustion, electromagnetic and buoyancy models were not selected, because those effect are assumed as negligible. Heat transfer model was set as total energy, following the recommendations at (ANSYS, 2020).

As was done at the inlet plane, the turbulent intensity for the whole domain needs to be initialized, initial conditions are needed for the simulations to begin. The intensity was set to 4%, 5% and 6% accordingly to the three inlet values (and 4,6 % too).

4.3.3.4 Turbulent and transitional model

SST $k-\omega$ turbulence model and the Langtry-Menter $\gamma-\theta$ transition model were selected to be used. Default settings were used, no changes on any parameter.

4.3.4 Run and Mesh Independence Study

The solver control tool (CFX-Solution) was used, together with ‘Parameter Set’ to perform a ‘Mesh Independence Study’. The aim of this study is to be sure that the final result is independence from the number of elements of the mesh, i.e., extra refinements of the mesh will not make any change on the results.

When increasing the number of elements, the solution varies and becomes closer to the analytical result, it can be done almost endless, so a criterion needs to be set to stop this process when the result is close enough to the analytical solution.

It is necessary to explain the difference between the terms ‘iteration’ and ‘iterative process’. An ‘iteration’ is the time the solver solves the transport equations for a cell on the mesh; an ‘iterative process’ is the name that was given to the cluster of iterations that are done until the convergence is reached for a particular mesh size. So, an ‘iterative process’ is a group of ‘iterations’.

This report is focused both into heat transfer and boundary layer transition. Following the insights obtained from (I. Jonsson S. D., 2020), a key parameter for both is the Heat Transfer Coefficient at the OGV blade surface, so this parameter was chosen for being checked after each ‘iterative process’ and observed through it the evolution of the results. SST model requires a y^+ value under 1. y^+ parameter has a critical influence on the boundary layer, and then in the heat transfer, so it was selected to study the convergence too. There are 3 walls on the domain: blade, hub and shroud, and convergence was studied for the 3 of them. Those two parameters are defined as ‘Quantity of Interest’.

The ‘Mesh Independence Study’ is about checking a parameter and observing its convergence. The parameters selected has a value that varies from cell to cell, in order to monitorize those parameters and plot them, they need to be area averaged, so the quantities of interest are:

- Area Average Heat Transfer Coefficient through the OGV Blade
- Area Average Y^+ over OGV blade
- Area Average Y^+ over OGV shroud
- Area Average Y^+ over OGV hub

The mesh needs to be improved after each ‘iterative process’, so the Global Size factor of the mesh was set as the parameter that changes. The bigger this parameter is, the finer the mesh became, i.e. higher number of mesh elements.

Several ‘iterative processes’ were carried out, trying different sets of parameters. Later on, it will be discussed how the different simulations were sorted out, but for the mesh independence study, only two simulations were studied:

- Constant wall heat flux through the blade (4% turbulent intensity, 1 cm length scale)
- Constant surface blade temperature (4% turbulent intensity, 1 cm length scale)

Before the simulations start to run there are several parameters that need to be adjusted. Adhered to (ANSYS, 2020) for this case, High Resolution is recommended for Advection parameter. High Resolution will increase Turbulence accuracy so was selected too. The solver can stop for three different reasons (apart from a failure): convergence criteria is fulfilled, maximum number of iterations are reached or the user decides to stop it. Quantities of interest need to be controlled manually, by observing the graphs until there is no variation, so the stop by user is the most appropriated system to be used. To make sure that the solver do not stop too soon, the maximum number of iteration is set to a high value, and the convergence criteria values are set really low (residuals and imbalances).

Timescale control is a delicate parameter, it affects to the velocity of the convergence of each iteration. A high value can cause the solution to become bouncy and a low value will make the solver run slow, being too time consuming and may lead to an accuracy lost. Because of the lack of information, a guessabout process was done, looking for the best agreement between time and accuracy. Low timescale factor values were used for the coarser meshes and high values for the finer meshes (values from 1 to 50 were used).

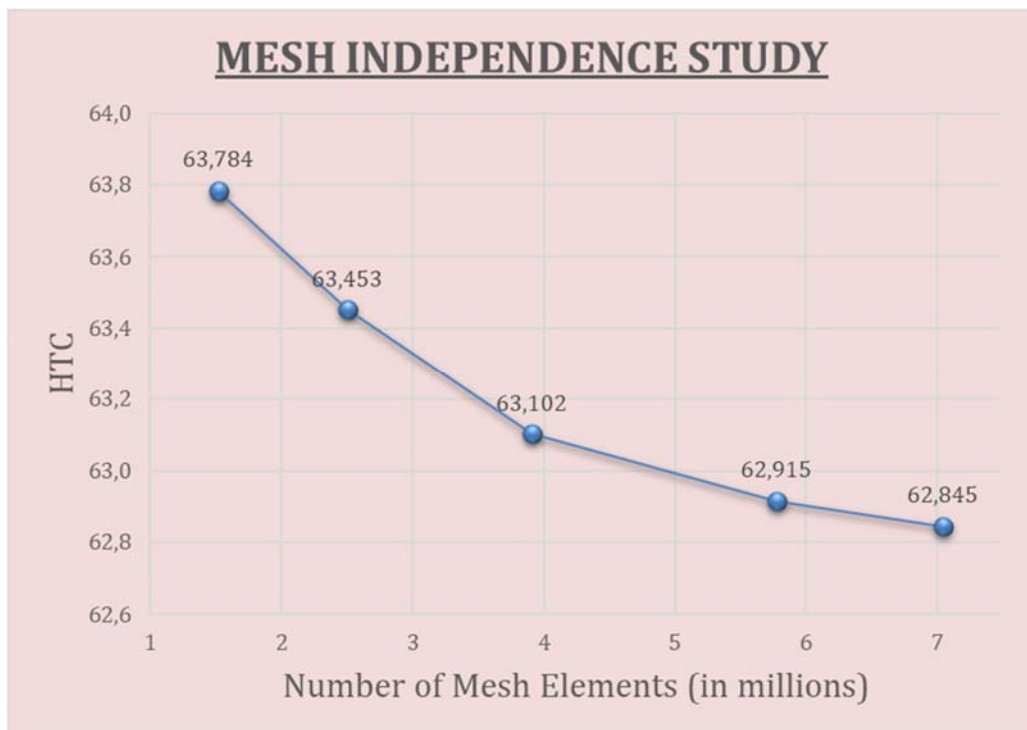


Figure 18. Convergence of Wall HTC Average value (constant temperature)

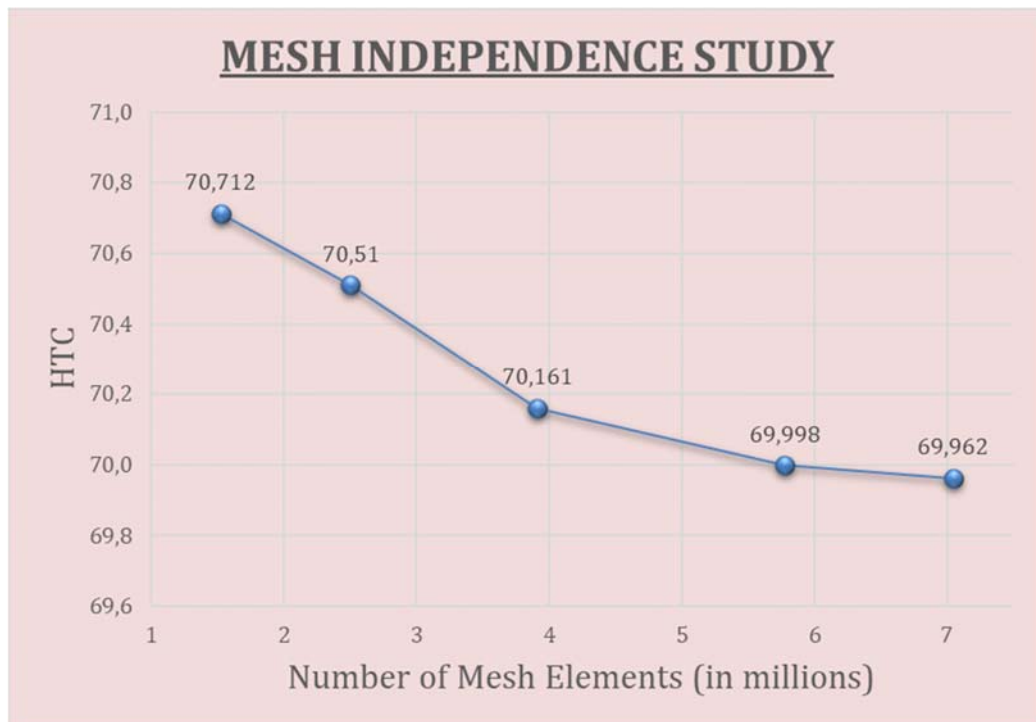


Figure 19. Convergence of Wall HTC Average value (constant wall heat flux)

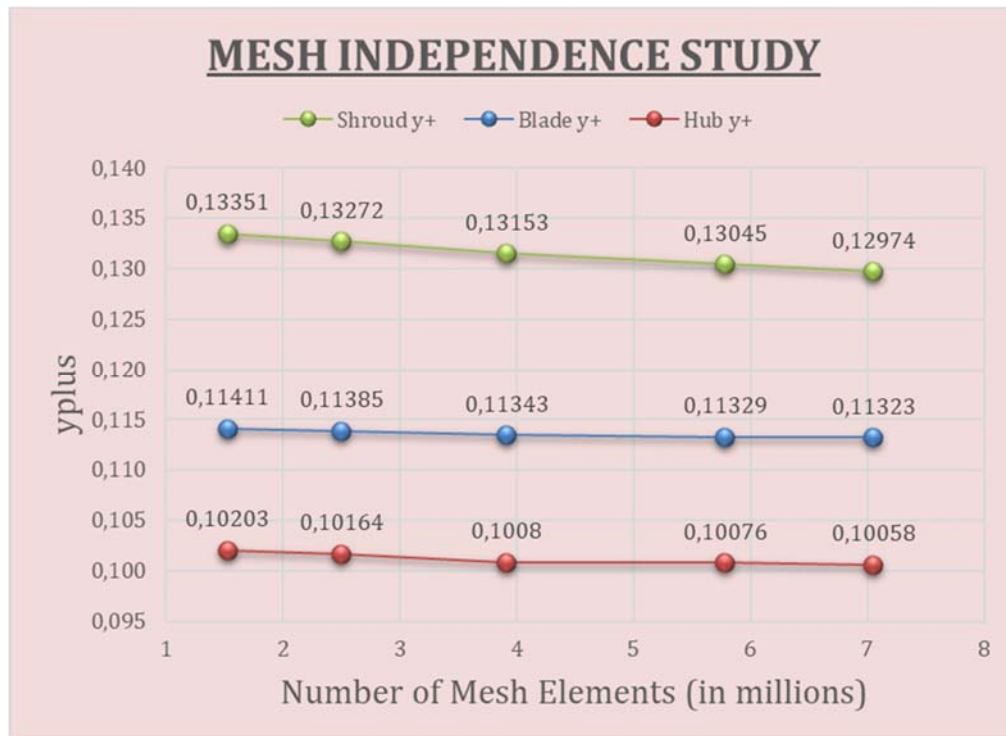


Figure 20. Convergence of y^+ Average value (constant temperature)

Two mesh independence studies were done, for the two cases mentioned before. Global Size Parameter is set, simulations are run until convergence criteria of the 'iterative process' are fulfilled; Global Size Parameter is increase, mesh refreshes, simulation run again, and criteria are check. This process is repeated until the variation of the average HTC from one 'iterative process' to the following is lower than a tenth (HTC results can be observed at Figure 18 and Figure 19, and at Figure 20 and Figure 21 for y^+).

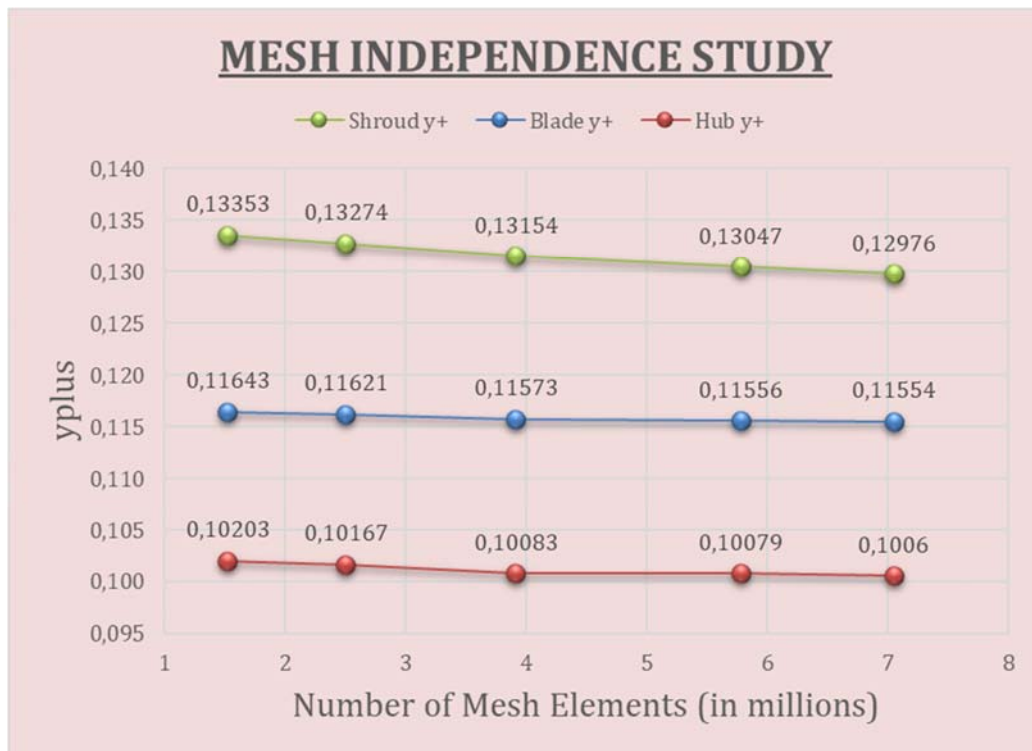


Figure 21. Convergence of y+ Average value (constant wall heat flux)

It can be observed that there is almost no variation for the y+ values, but there is a remarkable difference for the HTC values for both cases. The convergence criteria used was variation of a tenth, based on the pattern described by HTC (and y+ too) convergence can be assumed as 'reach'. Finer meshes will show different results, but the differences are expected to be negligible.

The convergence criteria for the iterative process is formed by 3 criteria related to residuals and imbalances. Residuals is a measurement of the local error when solving the transport equations, it means that each cell has a residual value for the 9 transport equations solved. Imbalances are global values that account for the conservation of the quantities evaluated by the transport equations over the whole domain. The criteria are:

- Root Mean Square Residual must be $1 * 10^{-5}$ or lower for each quantity (not bouncing) (Figure 28 to Figure 33)
- Imbalances under 1% for each quantity (Figure 26 and Figure 27)
- "Quantities of interest" are stabilized (Figure 22 to Figure 25)

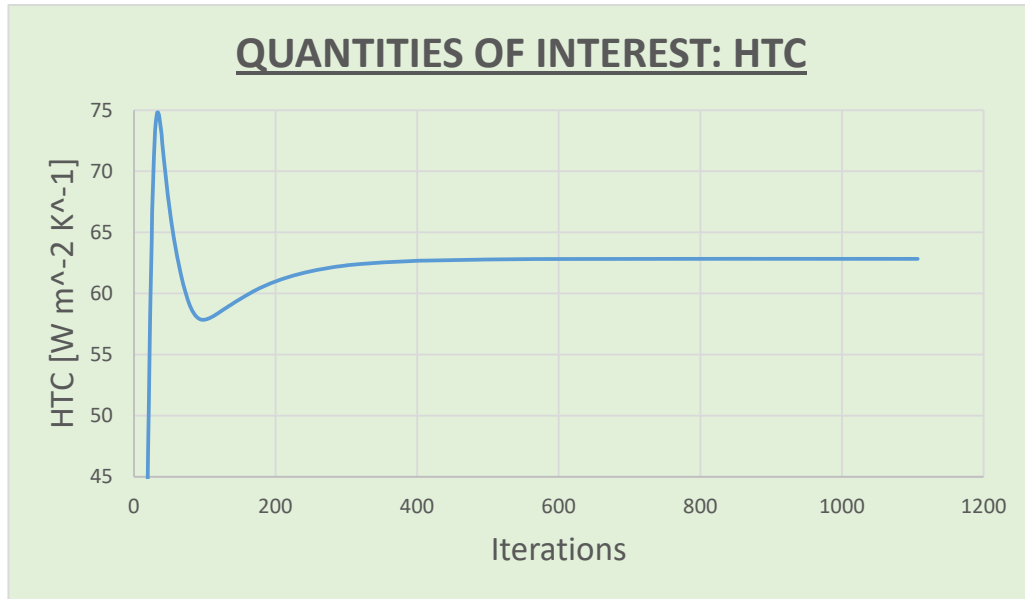


Figure 22. Evolution of Area Average *HTC* (constant temperature)

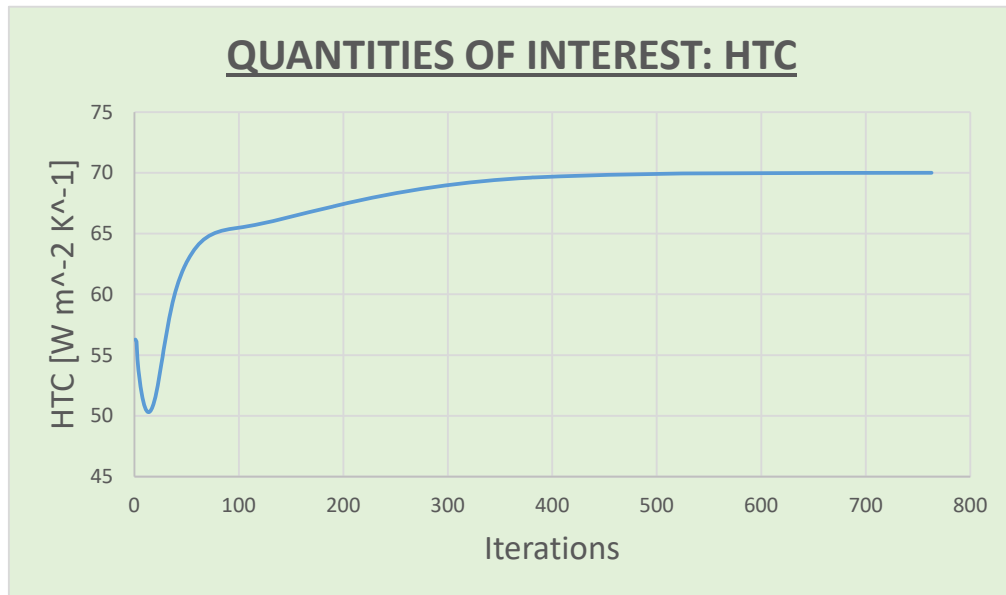


Figure 23. Evolution of Area Average *HTC* (constant heat flux)

It can be observed that the *HTC* value is around $63 \frac{W}{m^2 \cdot K}$ for the constant temperature case and around $70 \frac{W}{m^2 \cdot K}$ for constant wall heat flux.

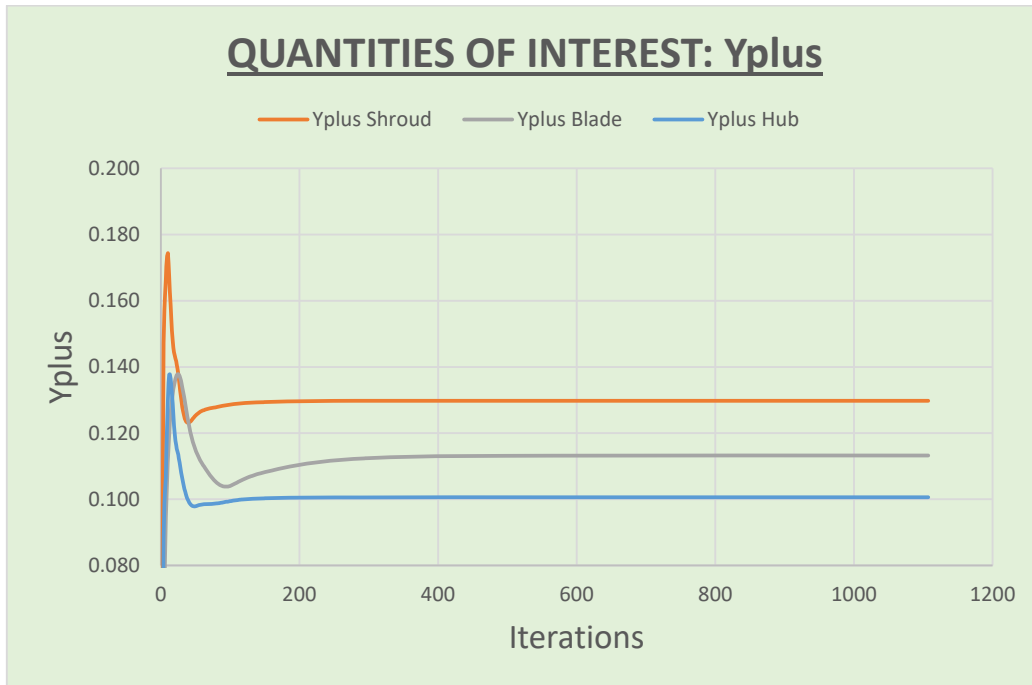


Figure 24. Evolution of y^+ (constant temperature)

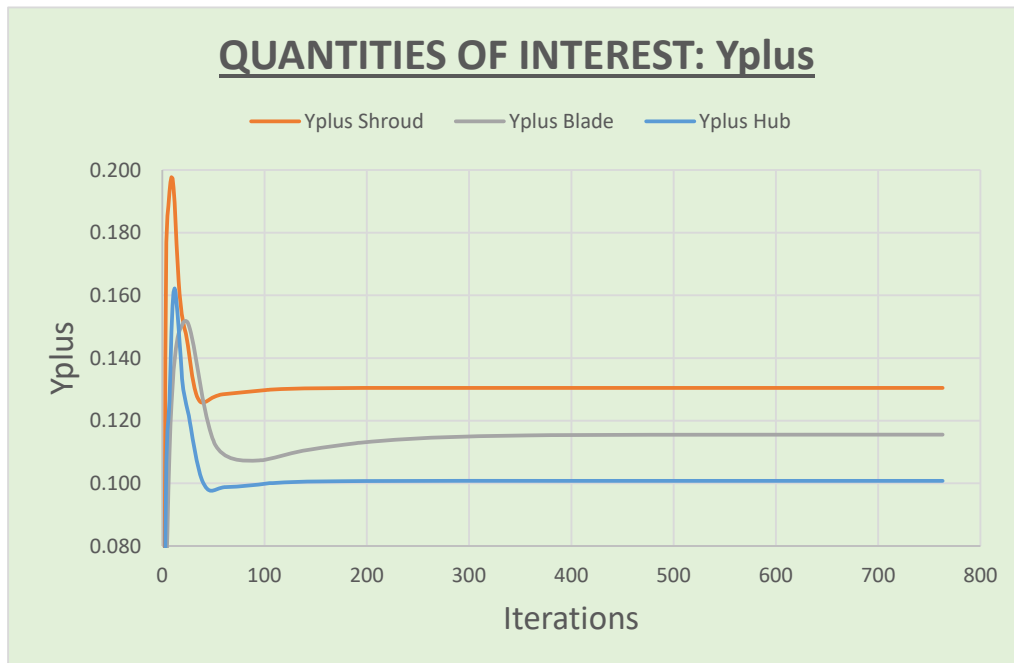


Figure 25. Evolution of y^+ (constant heat flux)

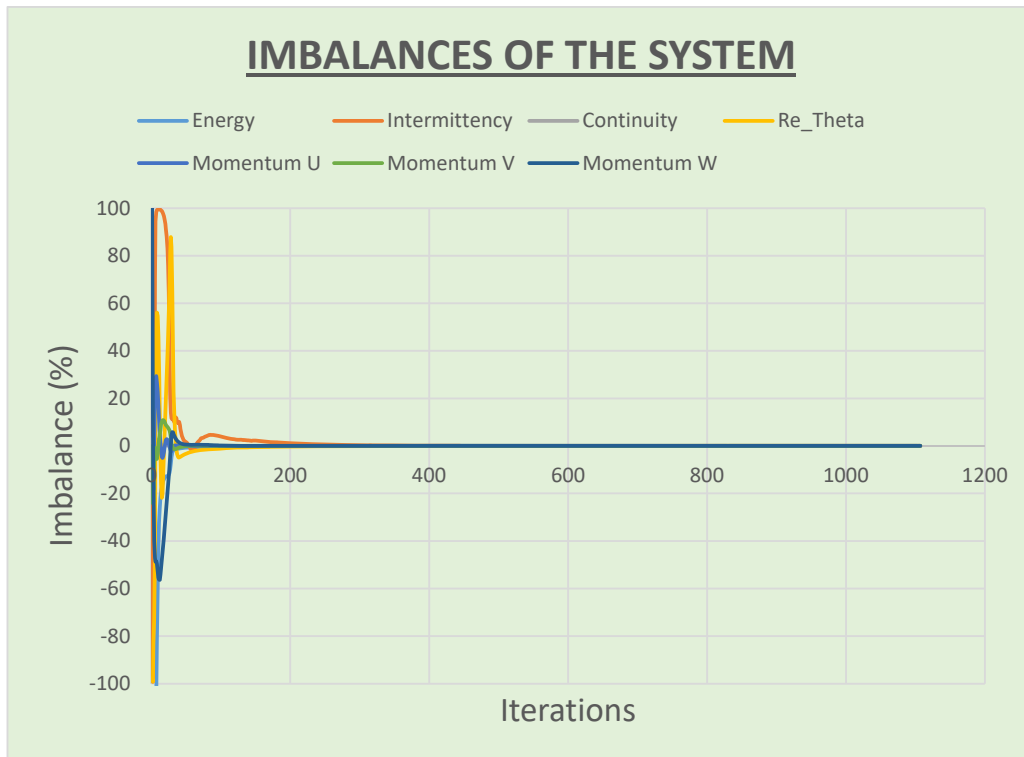


Figure 26. Imbalances (constant temperature)

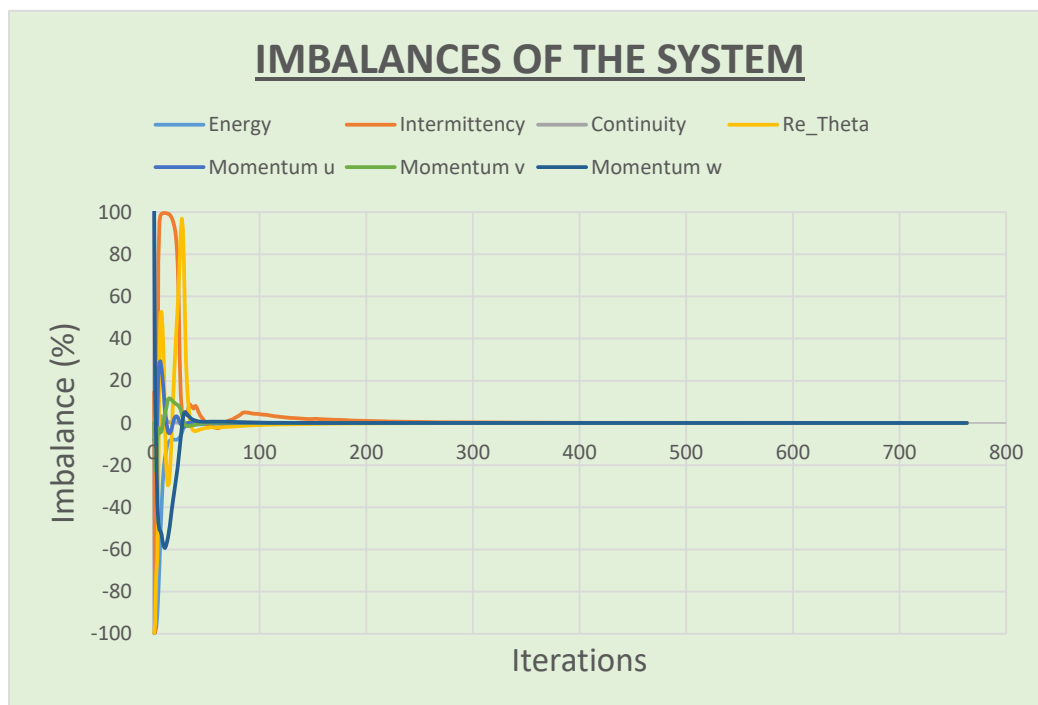


Figure 27. Imbalances (constant wall heat flux)

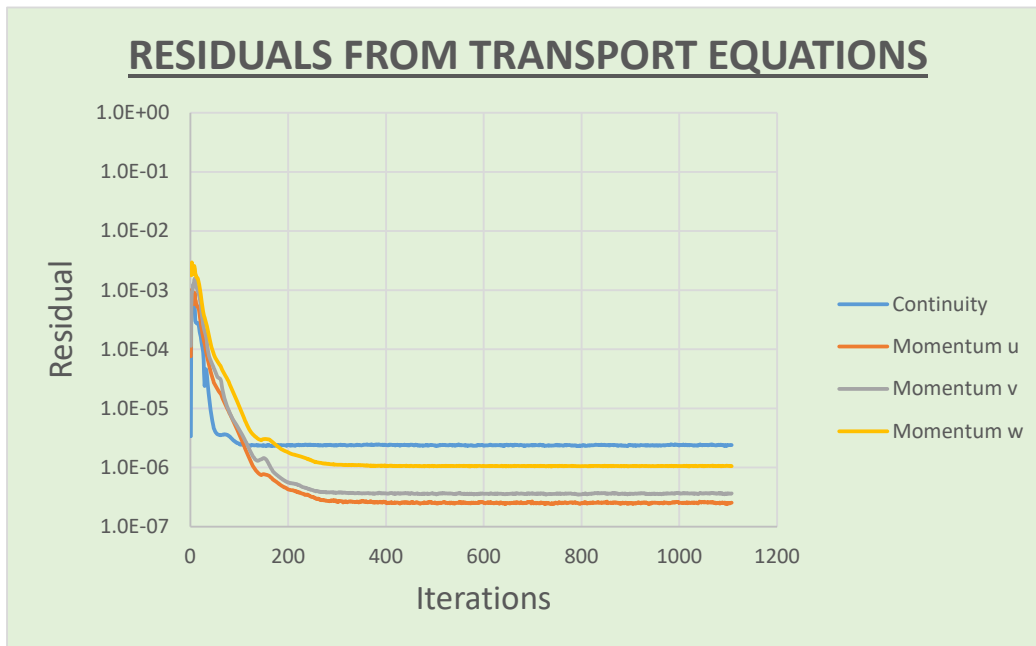


Figure 28. Evolution mass and momentum residuals (constant temperature)

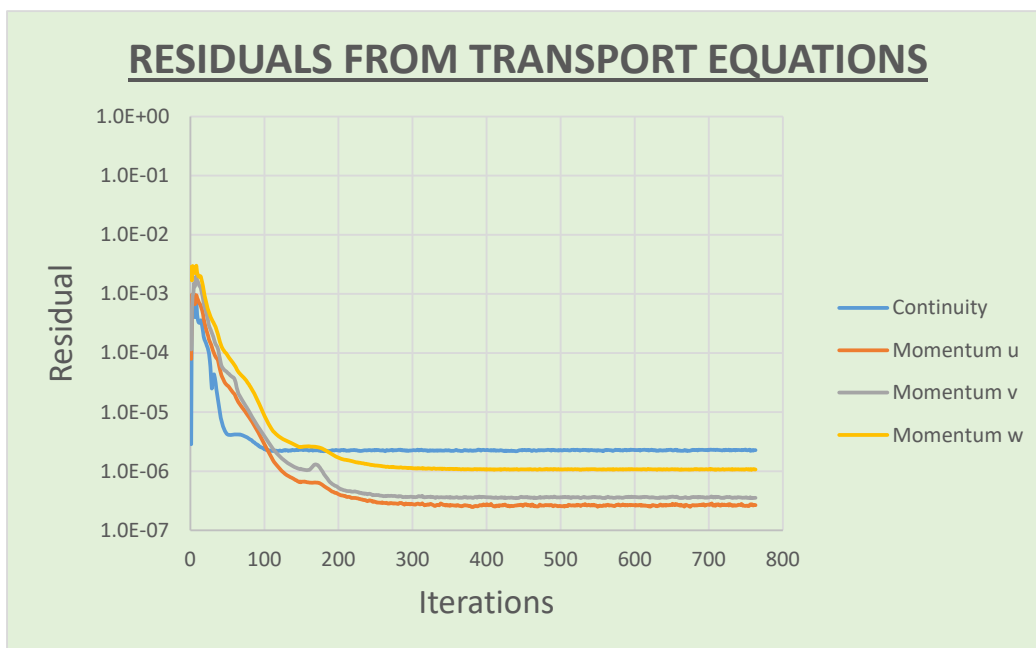


Figure 29. Evolution mass and momentum residuals (constant wall heat flux)

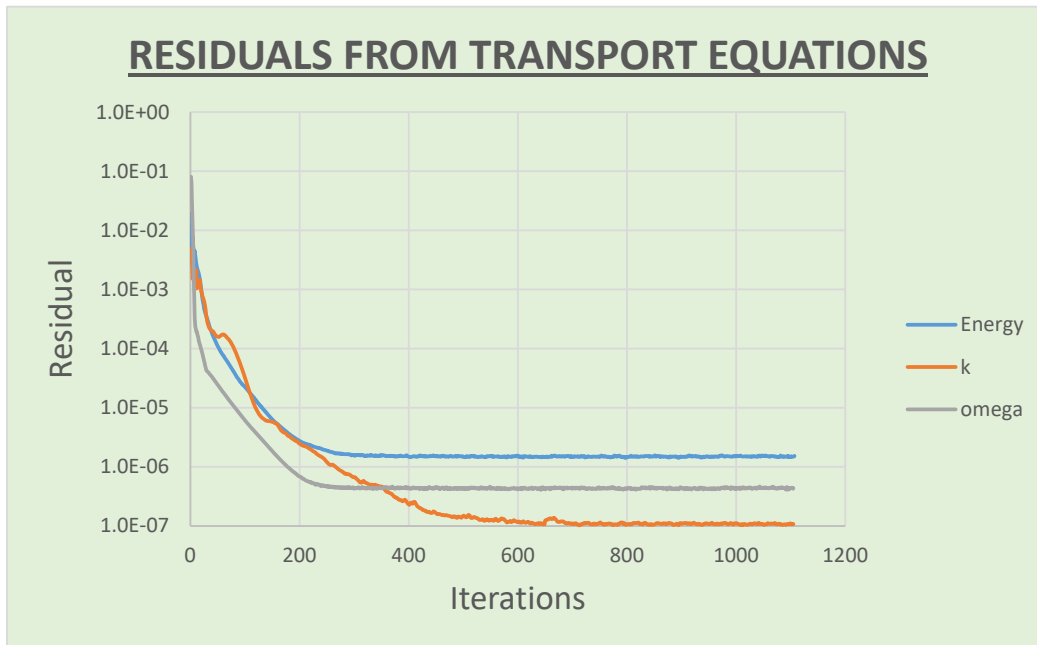


Figure 30. Evolution heat transfer and turbulent residuals (constant temperature)

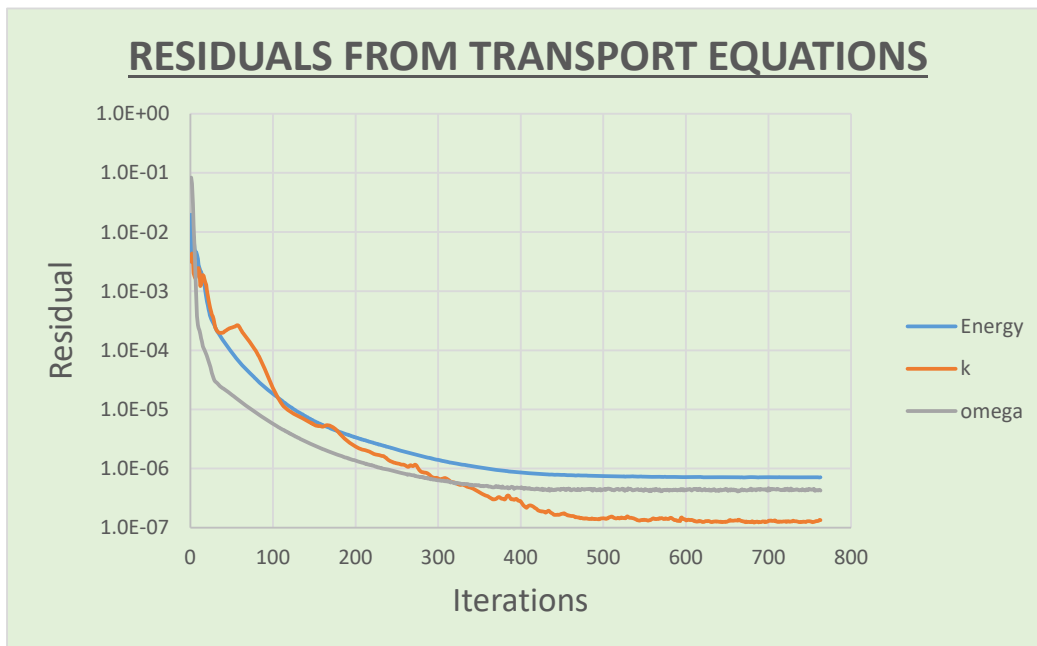


Figure 31. Evolution heat transfer and turbulent residuals (constant wall heat flux)

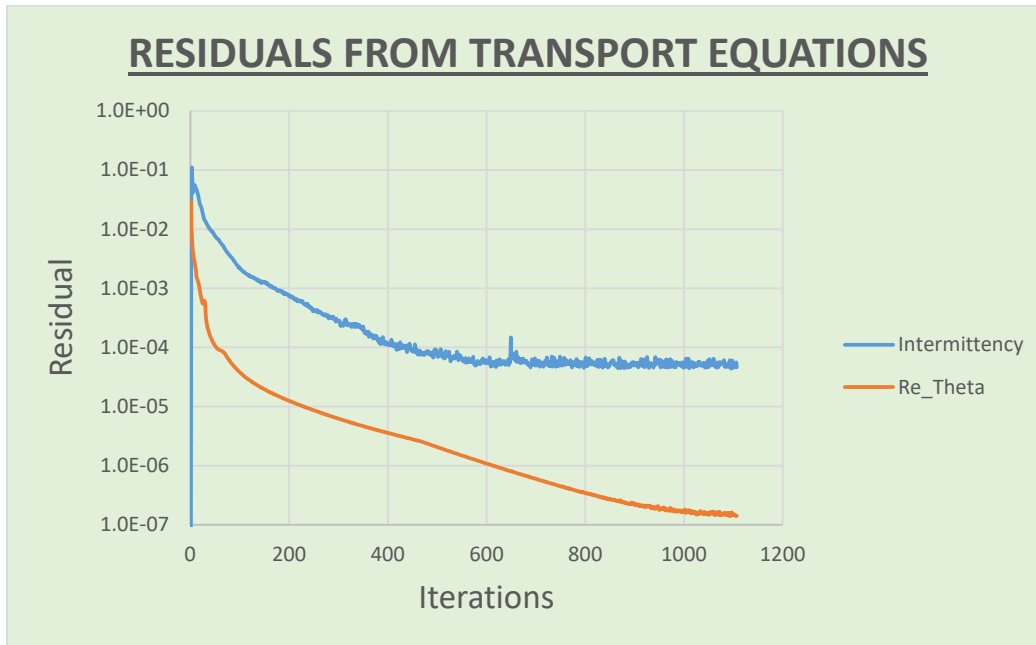


Figure 32. Evolution transitional residuals (constant temperature)

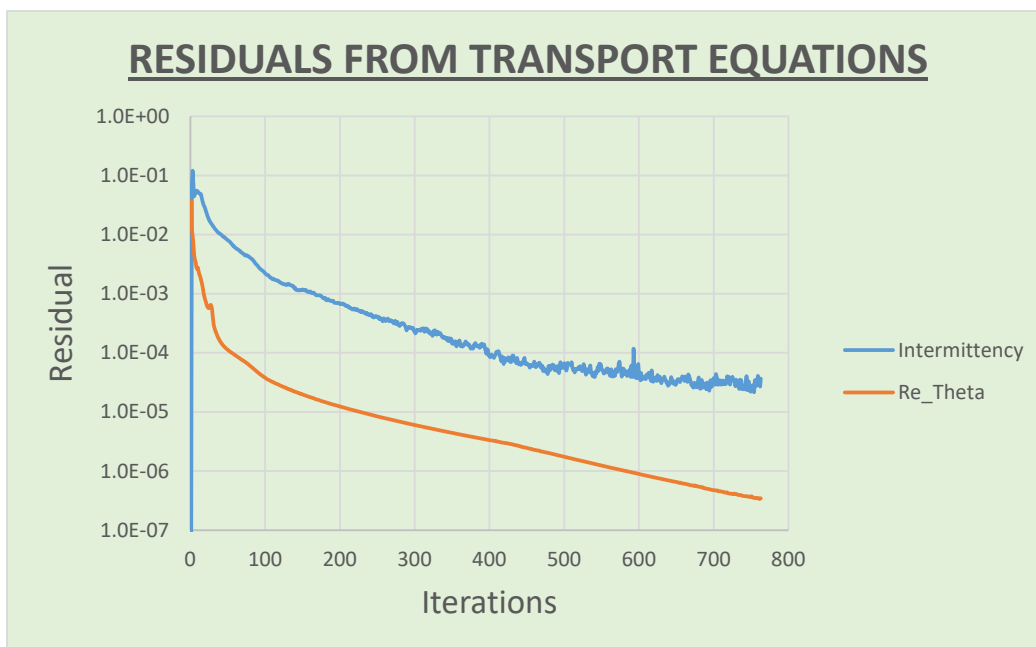


Figure 33. Evolution transitional residuals (constant wall heat flux)

It can be seen that all the residual values are stabilized with values under $1 * 10^{-5}$ except for intermittency. There is no noticeable difference between the two cases studied, speaking about residuals, imbalances or “quantities of interest”. Some ‘noise’ can be observed on the intermittency graphs from 300 iterations onwards.

5 Results

This section is divided in 2 subsections. Aerodynamic evaluation and aerothermal evaluation. Both subsections are mainly based on numerics vs experimental comparisons. Aerodynamics compare flow features like swirl angles, blade loading or turbulence decay. On the other hand, aerothermal, dive into the heat transfer over the blade, analyzing how the HTC is distributed all over the blade surface and examining the 2 simplifications (constant temperature and constant heat flux) done for modelling the heat transfer.

5.1 Aerodynamic evaluation

To get the results that are going to be shown in this section, several different cases were solved. As it was explained at “Running and Mesh Independence Study” the mesh size was modified over and over until reach convergence. For different meshes size different results were obtained, to illustrate the convergence of the data different aerodynamic properties are going to be compared.

On the first place, inlet will be checked, by the mean of contours and graphs that show the accuracy of the interpolation performed. Then, blade loading will be analyzed to check if the aerodynamics simulated correspond or not to the experimental data on the mid-stream area. Finally, the outlet plane will be examined, searching for deviations between numeric and experimental. All the numerical data and results obtained are for Reynolds number, Re approximately of 235K and a flow coefficient, $\phi = 0.622$

5.1.1 Inlet

Swirl angle is related to the velocity components that were used as input, so it will verify the accuracy of the interpolation previously performed. Another parameter that can help in verifying this exactitude is the total pressure and the derived total pressure coefficient.

5.1.1.1 Swirl angle

Ahead are presented two images, both plotted using Matlab tools. The first one corresponds to the experimental data, and the other one to the Ansys results (for the mesh size used on the last iteration before satisfying all convergence criteria). The same colorscale was used for both contours.

Comparing experimental and interpolated contours, an alike pattern is observed. Near the hub wall a pair of rotating vortices has been observed similar to the experimental results. These concordances is related to the exactitude of the interpolation performed, because, as said before, swirl angle is calculated based on two of the velocity components that were set as input data to the simulations on the inlet plane.

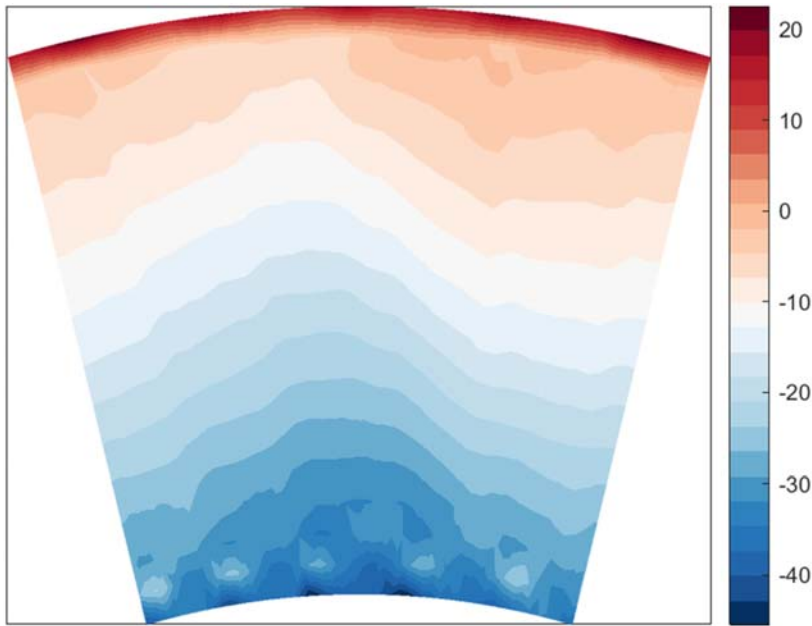


Figure 34. Swirl Angle at Inlet plane (Experimental)

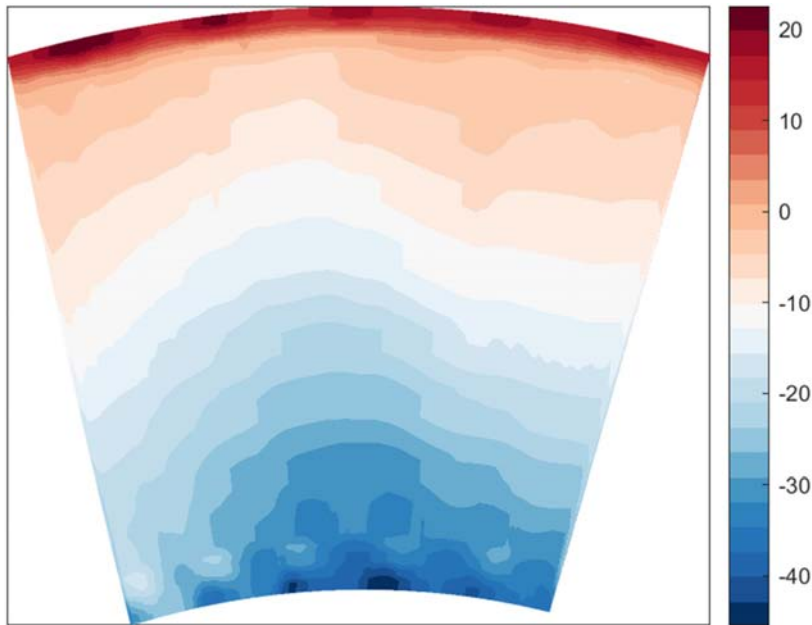


Figure 35. Swirl Angle implementation on the numerical domain

Some differences can be identified close to hub and shroud, it is caused by the interpolation, because the numerical domain is bigger than the experimental, and it leads to missing values close to hub and shroud (see Processing of experimental data). These discrepancies can be clearly observed on the dark red and dark blue areas close to the walls on the interpolated contour.

Apart from the contours comparison, another evaluation was performed by the mean of a graph that circumferentially averaged the swirl angle at the inlet. Interpolated and experimental data are compared.

As can be seen at Figure 36 the swirl angle distribution is similar for interpolated and experimental for 0.05- 0.9 span. The swirl angle is over a wide range while entering the OGV. The discrepancy below 0.5 span is possible due to difference in the inlet averaging method while obtaining the swirl angles in the experimental data and CFX (interpolated).

Here it can be observed that the experimental data do not reach neither the top nor the bottom of the graph. 0 span correspond to the ‘real’ hub position and 1 to the shroud. As said before, the experimental data could not be got close to the walls, that is the reason for the lack of experimental points on those two areas, and it motivated the data interpolation that was performed.

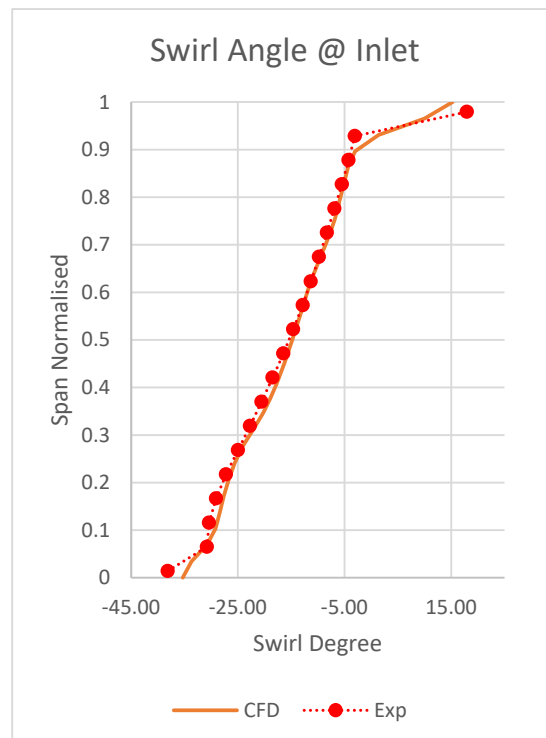


Figure 36. Graph comparing Swirl Angle at Inlet (CFD refers to interpolated)

5.1.1.2 Total pressure and total pressure coefficient

A procedure similar to the swirl angle evaluation will be followed to perform the total pressure study. A contour comparison is done for the total pressure and total pressure coefficient will be studied by the mean of a plotted curve with circumferentially averaged data. The same colorscale was used

Both numerical and interpolated contours has the same pattern. Comparison between numerical and experimental shows an aike pattern and a concordance on the color scale values.

The wakes generated by the 6 NGV blades that are located upstream of the inlet plane can be observed on both numerical and interpolated contours.

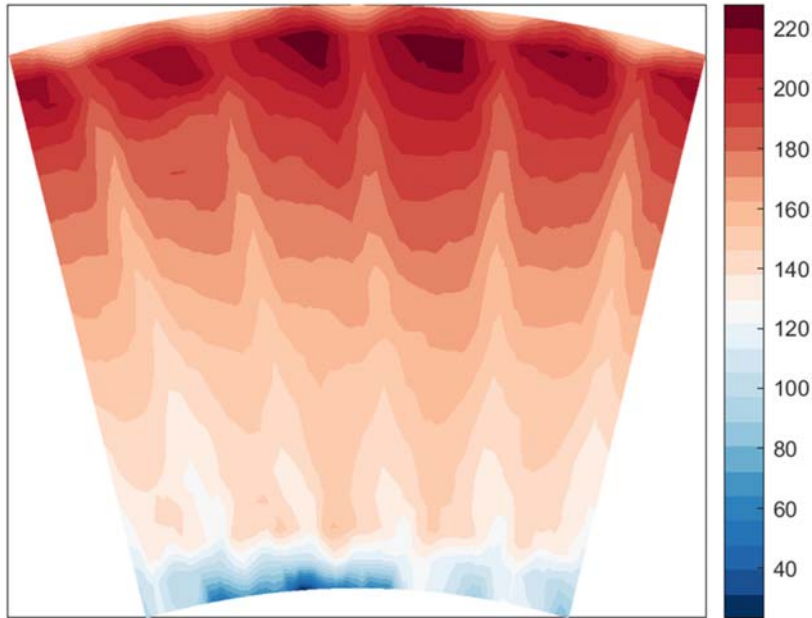


Figure 37. Total Pressure at Inlet plane (Experimental)

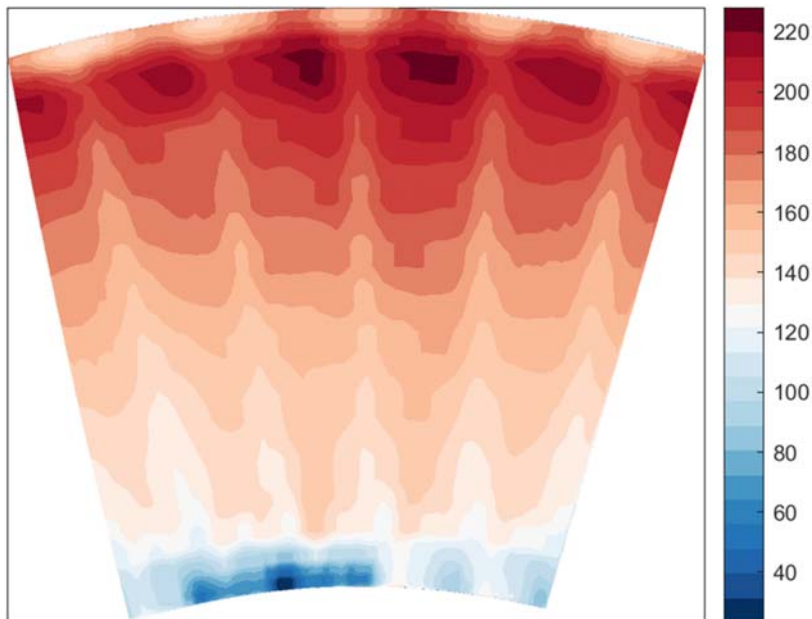


Figure 38. Total Pressure implementation on the numerical domain

Figure below shows radial distribution of total pressure coefficient. The interpolated result (averaged by Ansys CFX of total pressure coefficient is in good agreement with the experimental data except the points near the hub (0.0-0.1) and near the shroud (0.9-1.0).

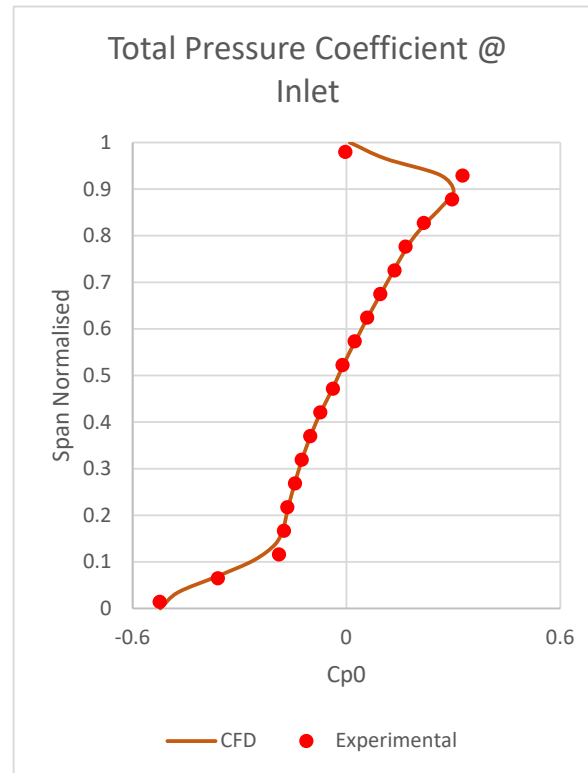


Figure 39. Total Pressure Coefficient comparison at Inlet

An offset can be observed in Figure 39. Due to extrapolation of the experimental data at inlet as a prerequisite to run the simulation, an offset of 2 Pa in Static Pressure Reference and 3 Pa in Total Pressure Reference has been inserted. This offset into the area average inlet values can be ignored as it is caused only due to extrapolation.

5.1.2 Blade loading

Previously inlet was analysed, ahead outlet will be. Here, the ‘midspan’ region is analysed by taking a look into the blade loading. It is necessary to match the numerical and experimental blade loading as good as possible, because it tell about the acceleration rate which is a primary flow effect for the transition onset on the suction side.

There is no ‘interpolated’ data here, so a comparison between experimental and CFX results (numerical) were done. In general, the blade loading between the numerical and experimental are nearly coherent but the numerical results are underloaded at the suction side for all the spans.

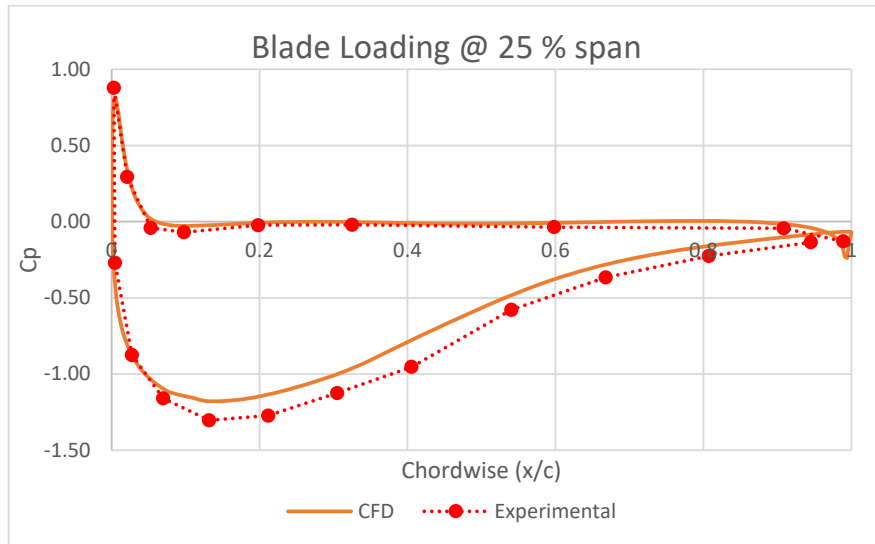


Figure 40. Blade loading comparison at 25% span

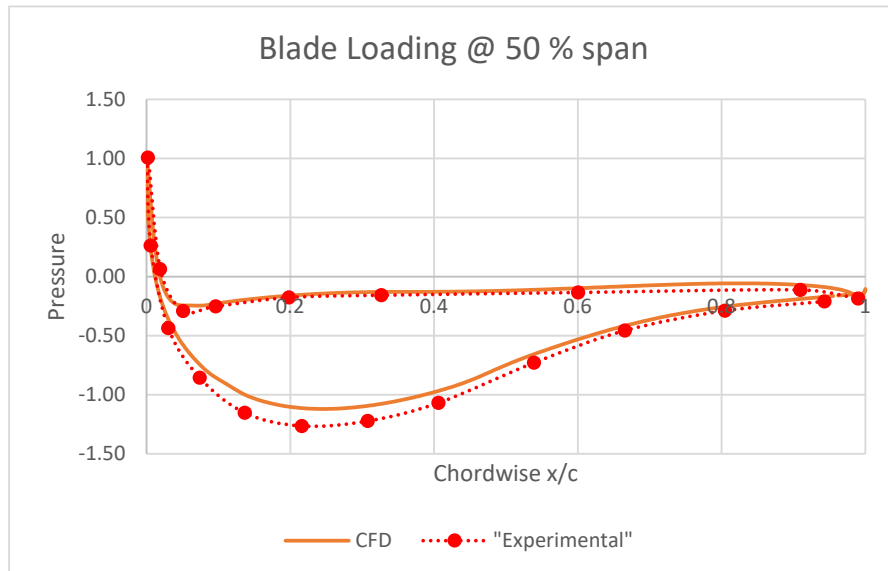


Figure 41. Blade loading comparison at 50% span

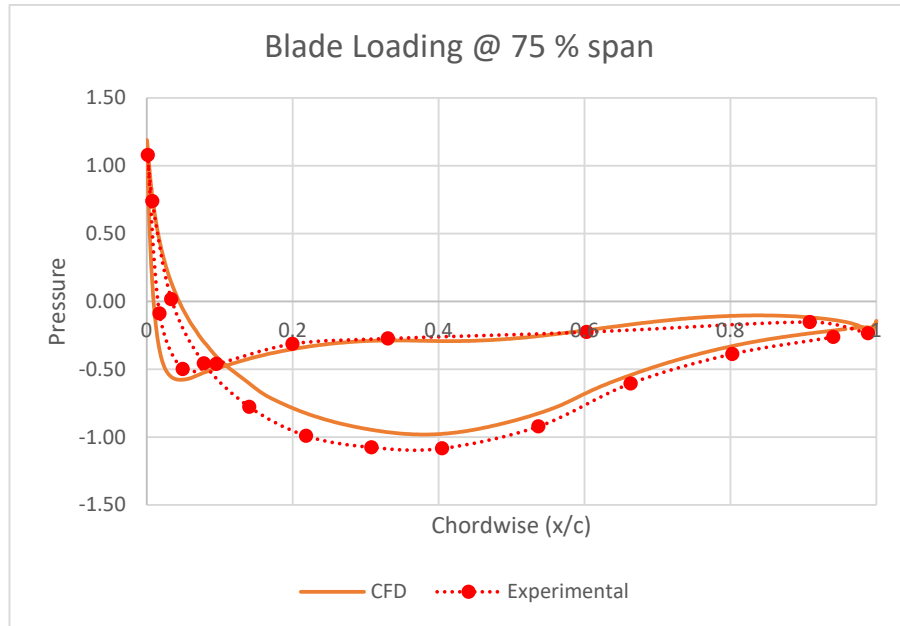


Figure 42. Blade loading comparison at 75% span

Potential reasons for the observed blade loading could be that the static pressure is too high which can be seen at inlet and outlet, which is possibly causing a pressure gradient in the numerical simulation which is different from the experimental observation. The effects are predominant at the trailing edge and the biggest discrepancies are observed near the suction peak.

High outlet pressure could be due to the fact that the inlet plane might be slightly off in position of the flow condition, and due to time constraint the simulation was done on a 2D plane instead of a radial plane (I. Jonsson V. C., 2020). Due to this, the features influencing the performance of the blade are averaged out, during averaging the inlet profile.

In general, the blade loading at midspan is has a good agreement between numerical and experimental values.

5.1.3 Outlet

Experimental data from the evaluation plane have been compared to the numerical results. Same procedure than inlet is followed, but adding a wake analysis.

5.1.3.1 Swirl angle

First of all, it is necessary to remind that the velocity component were not used as input data for the outlet (only static pressure), so in this section interpolation comparison is not done. Here results from Ansys CFX (numerical) are being compared with the experimental data.

Ahead are presented two images, both plotted using Matlab tools. The first one corresponds to the experimental data, and the other one to the Ansys numerical results (for the mesh size used on the last iteration before satisfying all convergence criteria). The same colorscale was used for both contours.

Comparing experimental and interpolated contours, an alike pattern is observed, the wake due to the OGV blade is captured. Some differences can be observed.

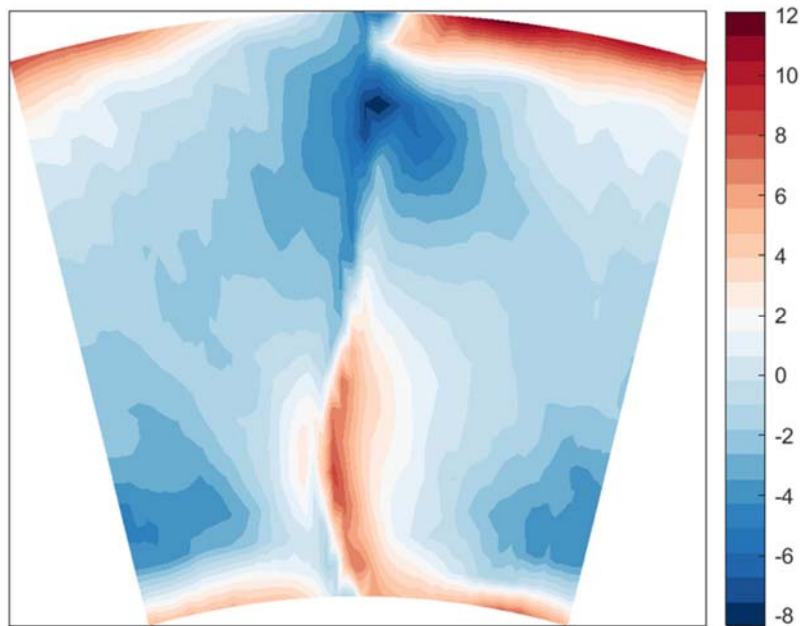


Figure 43. Swirl Angle at Outlet plane (Experimental)

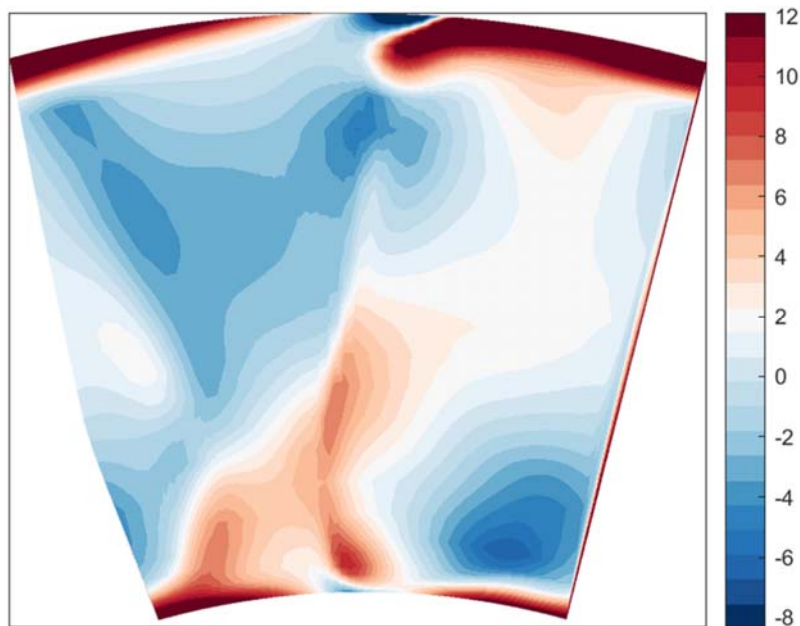


Figure 44. Swirl Angle at Outlet plane (Numerical)

Those differences are:

1. Red line on the right side of the experimental contour from the hub to the shroud. Turbogrid created an outlet plane that is not completely radial, it is formed by 2 lines (a vertex can be observed on the left side), it was not possible to solve this issue, and when plotting, it cause the creation of this 'artificial' line. It is not observed on the Ansys visualizer, it do not correspond to the results, it was created when plotting. This same issue can be observed on all the numerical outlet contours.
2. Hub and shroud discrepancies caused by the experimental data, which do not cover the areas close to the walls because of limitations when measuring. The experimental colorscale was used for plotting both contours, so those dark red areas close to the walls on the numerical contour correspond to values over 12 degrees predicted by the software but not captured on the experimental.
3. Related to the last point, it needs to be pinpointed that the tip leaking effect was not considered on the simulations, so it is another reason for the discrepancies clos to the shroud. It can be observed that shroud discrepancies are bigger than hub's.
4. A blow close to the hub, on the suction side (left side), can be detected, it could be caused because of the removal of the outlet passage, leading to a stiffer domain (same as blade loading).

In Figure 45 we have the spanwise distribution of swirl angle at the outlet. As explained above, there is a discrepancy near the hub and the shroud region. Aerodynamic purpose of the OGV is to de-swirl the flow, it can be observed that the average swirl between 0.1-0.9 span varies from between -1.25 to 1.45 degrees.

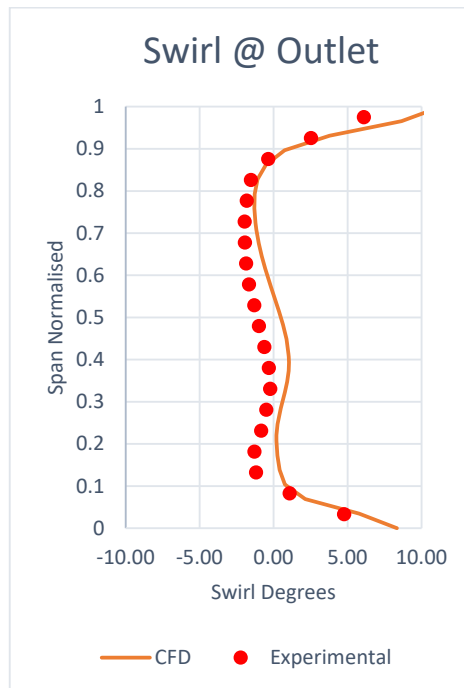


Figure 45. Graph comparing Swirl Angle at Outlet

Comparing the numerical outlet swirl, it is observed that the simulations underpredicts the swirl near the midspan. Hence the average turning at midspan is considerably lower for numerical results, and similar trends was observed in the blade loading. As mentioned in Section 5.1.2, in earlier simulations radial profiles have been used for previous simulations (I. Jonsson V. C., 2020), which is a possible reason for the difference in swirl angle at midspan.

5.1.3.2 Total pressure and total pressure coefficient

Comparison between numerical and experimental shows a similar pattern. The same differences that for the swirl angle are observed (see 5.1.3.1), but in this case with values under 50 Pa on the dark blue areas.

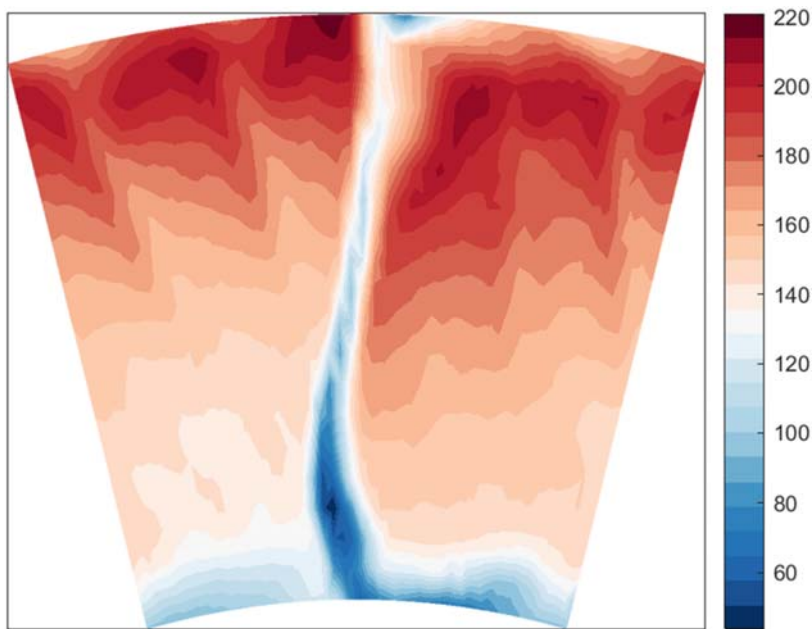


Figure 46. Total Pressure at Outlet plane (Experimental)

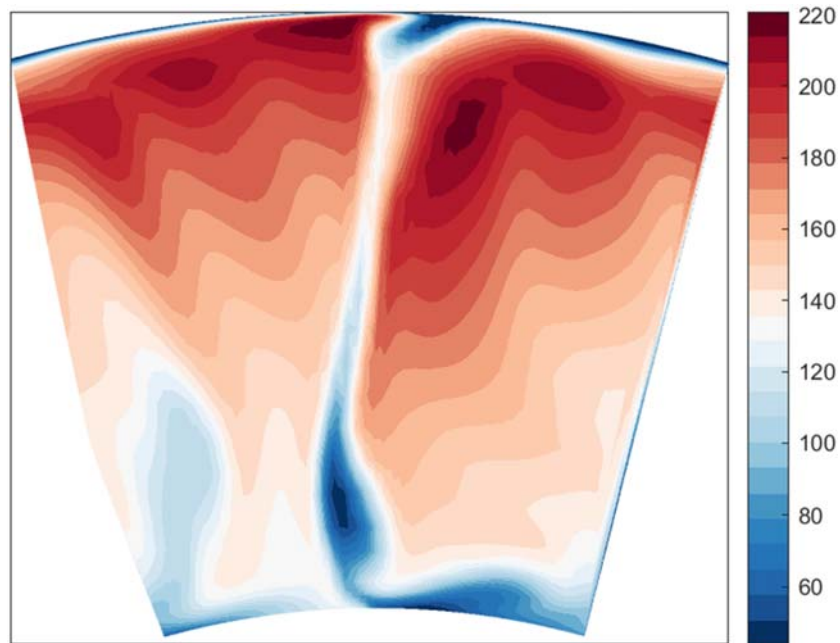


Figure 47. Total Pressure at Inlet plane (Numerical)

The wake generated by the OGV blades can be observed on both numerical and experimental contours, but numerical slightly overpredict the wake size caused by the blade.

Figure below shows radial distribution of total pressure coefficient. The numerical result of total pressure coefficient is in good agreement with the experimental data except the points near hub region and near the shroud (0.9-1.0) possibly due to extrapolation error and also, due to the discrepancy caused by the offset of 3 Pa in total pressure.

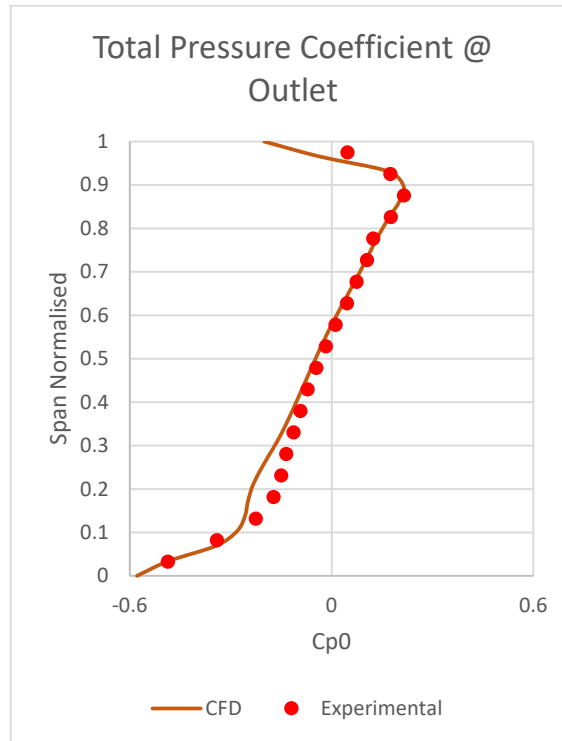


Figure 48. Total Pressure Coefficient comparison at Outlet

5.1.3.3 Wakes

Wakes are analysed with total pressure coefficient contours from the downstream. Fine and rough mesh agrees in both color scale and shape.

The same effect as for the total pressure and swirl angle can be observed, i.e.: there is no agreement close to the hub and shroud, blue line on the right side created when plotting, blow on the suction side close to the hub and numerical overprediction of the wake side.

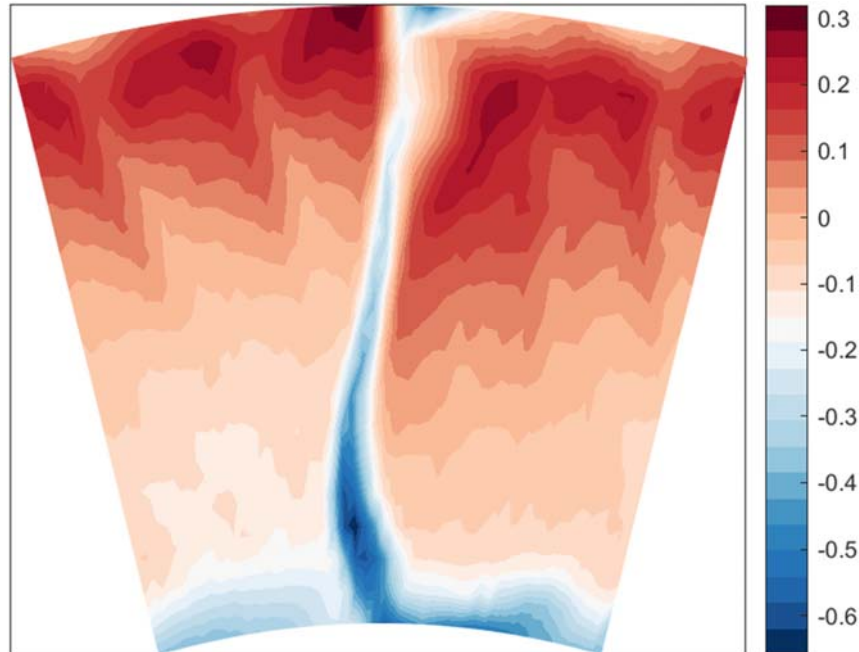


Figure 49. Wake analysis at Outlet plane (Experimental)

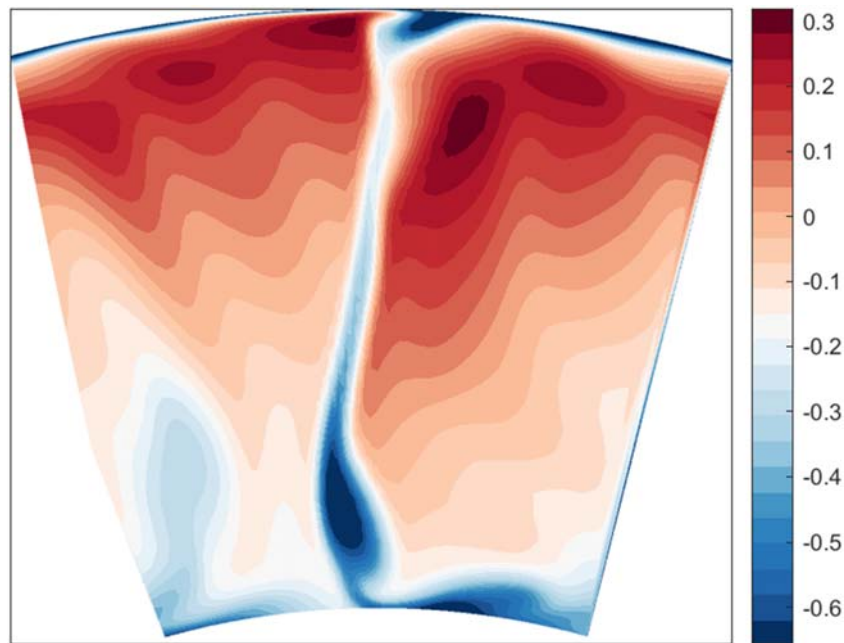


Figure 50. Wake analysis at Inlet plane (Numerical)

It can be observed that the wakes in both rough and fine mesh are overpredicted and wider near the hub possibly due to hub strong blade loading. The tip leakage effects propagates downstream, which can be one of the reasons that the wake width is underpredicted near the center and upper spans. But overall flow redistribution is fairly agreeable to the experimental data.

5.1.4 Turbulence decay at freestream

As explained before (see 3.5.4.2), turbulence decay is the most important parameter (studied on this report) when trying to capture transition onset location.

The air flow that goes out of the turbine stage has a 4,6% turbulent intensity level, and there is a decay because of the losses of turbulent energy due to the creation a boundary layer around the blade. This decay was measured experimentally by (I. Jonsson S. D., 2020).

One key parameter when running the simulations is eddy length scale, it is a parameter that is set together with the turbulent intensity, and it answer to the size of the biggest eddies on the turbulent flow. There was not reliable experimental data for this length scale, so an iterative process was done, starting with a value of approximately 50% of the pitch of the last LPT stage (1 cm).

As a first approach, 3 different cases were run with 4%, 5% and 6% turbulent intensity, using that value of 1 cm for the length scale (Figure 51). As it can be seen, the curve that better fits the experimental data is for the case of 4% turbulent intensity. The x/c location 0 represents the Leading Edge and 1 represents the trailing edge.

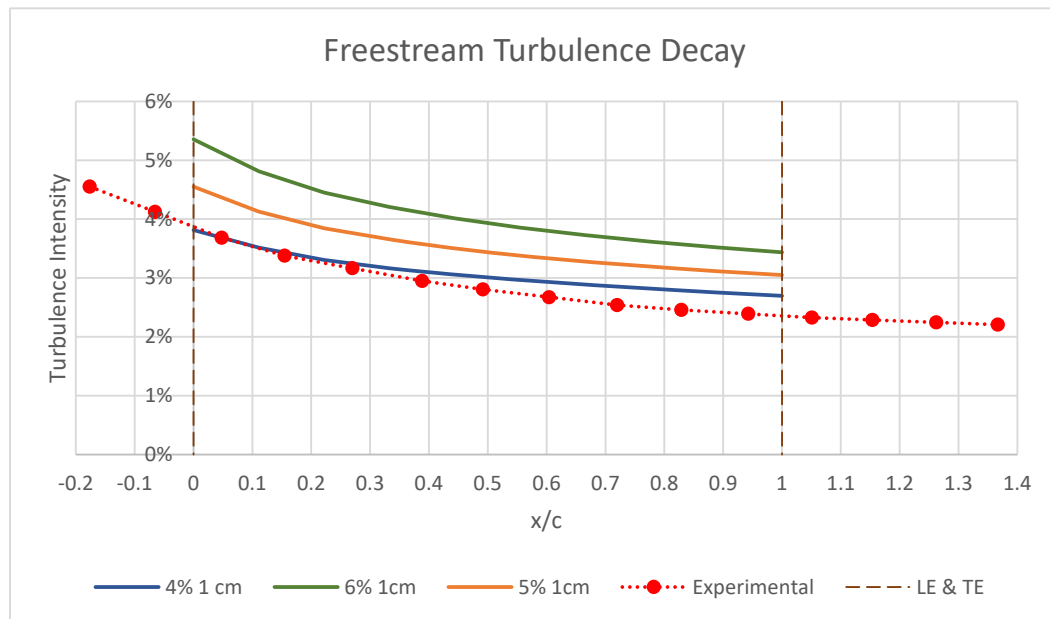


Figure 51. Turbulence Decay, first approach

Further investigation were done, and more length scale values were tried (between 0.5-1.5) to attain a more optimal turbulence decay. Based on Figure 55, 4% turbulence intensity was considered for this purpose and in Figure 56, the decay for 1 cm and 0.8 cm are observed.

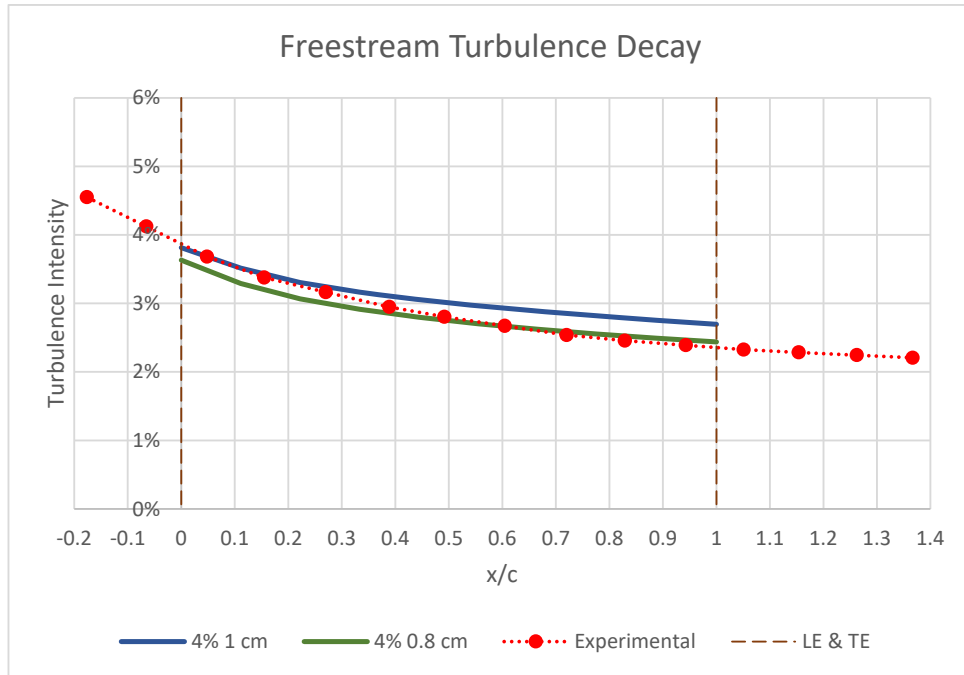


Figure 52. Turbulence Decay with different Length scales

The case with 0,8 cm fits better the experimental curve from 0,44 to 1 x/c, and 4% 1 cm curve fits better near the leading edge.

To get the transition onset position correctly, the freestream turbulent parameter should be as close to experimental as possible on the area that goes from the leading edge to the transition onset (because it is there where the freestream turbulent energy is transmitted to the boundary layer), based on the experimentals between 0 (leading edge) and 0,42 (expected transition onset location based on (I. Jonsson S. D., 2020)) streamwise location. It is observed that for the 4%, 1 cm case, the laminar and transitional regions match comparatively better.

By changing the turbulent intensity to 4,6% and trying other values for the length scale parameter, a better approach to the experimental curve can be achieved, but on this thesis, no further effort was dedicated due to time constraint of the project.

5.1.5 Transition onset (aerodynamic evaluation)

Transition onset refers to the position where the laminar region ends, and transition region starts. The turbulent energy inside the boundary layer increase (creating eddies) because of the transmission from the freestream flow, and it causes the laminar flow to become transitional and later turbulent. The transition onset is defined as the point where the enhancement of turbulent energy causes an increase in the HTC (refer to Section **Error! Reference source not found.** for further information).

On this section the heat transfer is analyzed for the constant blade temperature case, changing aerothermal parameters like turbulent intensity and eddy length scale. Only suction side is analysed, pressure side was out of the scope of the present report. Another section regarding only aerothermal parameters is present later on this report.

5.1.5.1 Suction side

Same procedure than for the turbulent decay is follow; first, numerical results with different turbulent intensity levels are compared against experimental data. Later on, changes on the eddy length scale are analyzed.

The decay at low x/c values correspond to the laminar region (boundary layer), the increase in heat transfer coefficient represents laminar-turbulent transition, and the slight decrease at high x/c values relate to the turbulent region. The onset transition is located on the lower HTC value at the end of laminar region, where values start rising again. The highest point at the transitional region is the end of transition. The length of transitional region is the distance between nset at end.

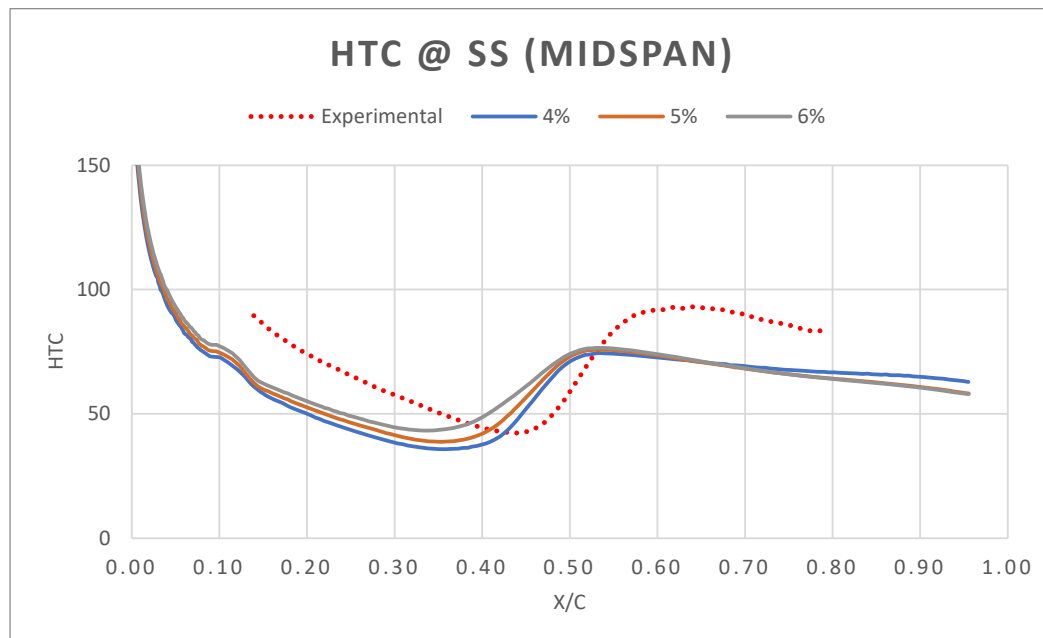


Figure 53. HTC Comparison at Suction Side with different Intensities

The effects of transition on HTC distribution was studied for different turbulent intensities with 1 cm length scale. As it can be seen in Figure 53, with increasing turbulence intensity, the transition region moves further upstream of the vane. Based on the selection of 4% free-stream turbulence intensity from the previous section, it can

be noticed in Figure 53 that the 4% curve is the closest to the transition onset position (0,44 x/c on experimental and 0,37 x/c on numerical 4%).

Moreover, the effect of transition was studied when different length scales were considered for the 4% turbulence intensity case. In Figure 54 it is observed that higher length scale triggers an early transition.

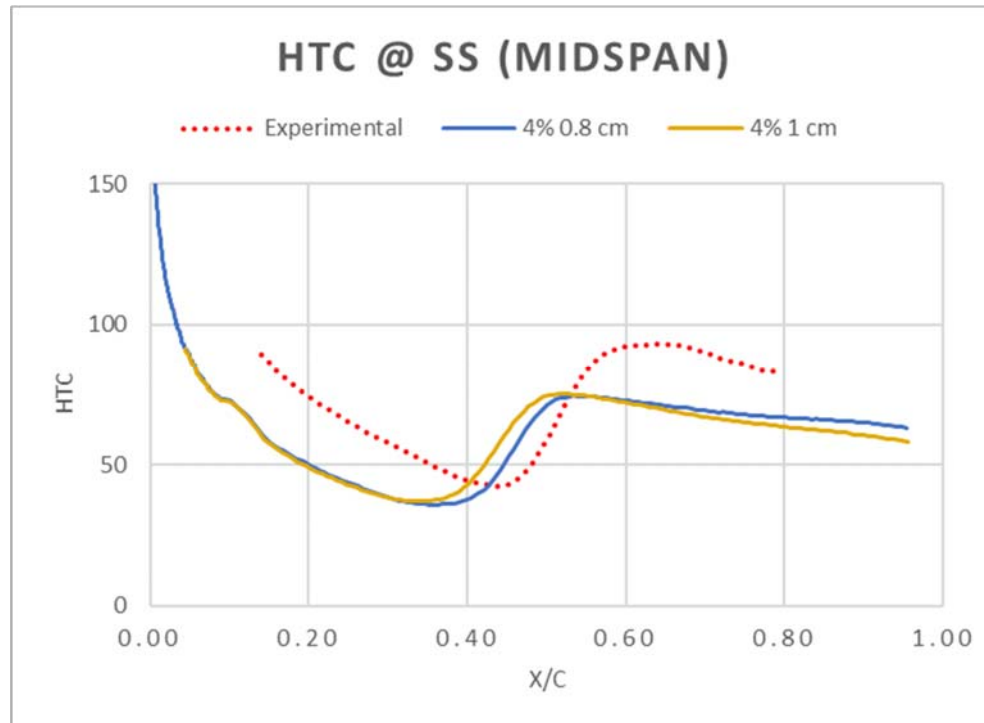


Figure 54. HTC Comparison at Suction Side with different length scales

The offset that exists for all the cases, means a low HTC over the laminar area, what also means a low turbulent energy. A natural transition requires of instabilities to be created and amplified, a by-pass transition is caused where the freestream turbulent is really high locally and the separated flow transition is caused by adverse pressure gradients. Numerical results show a lower HTC values and a shorter laminar area compared to the experimental, so natural transition is not likely to happen. The freestream turbulent levels are not high, there is no shape edges on the airfoil and there is no peak on the turbulent pattern, so by-pass transition is not likely too.

Separated flow transition can explain those two different patterns, becoming transitional and turbulent around the same location.

Due to simplified simulation (constant blade temperature) the results show lesser confidence, when compared to the experimental data. Increasing the complexities of the simulation might result in capturing a more accurate conjugate heat transfer.

5.2 Aerothermal evaluation

In Section 5.1, looking at the mid-span, the blade loading and wake analysis results indicate that the aerodynamic flow field has been captured quite reliably. Aerothermal properties were investigated for the similar domain. Regarding the results near the endwalls, it is slightly difficult to discuss, but on the mid span, the aerothermal evaluation is in good agreement.

5.2.1 Heat transfer coefficient over the blade

The aerothermal performance is evaluated by comparing (experiment vs numerical) the amount of heat that is transferred between the freestream flow and the blade surface (for the constant blade temperature case). HTC is the parameter choose to show that comparison. Figures below show comparison of contours of Heat transfer coefficient between Numerical and experimental results for both suction and pressure sides for a constant blade surface temperature case.

First, suction side is analysed. On the second place, pressure side.

HTC
Contour 1
200.0
180.0
160.0
140.0
120.0
100.0
80.0
60.0
40.0
[W m⁻² K⁻¹]

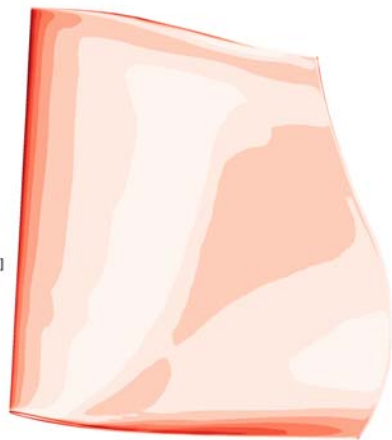


Figure 55. HTC profile at the Suction Side

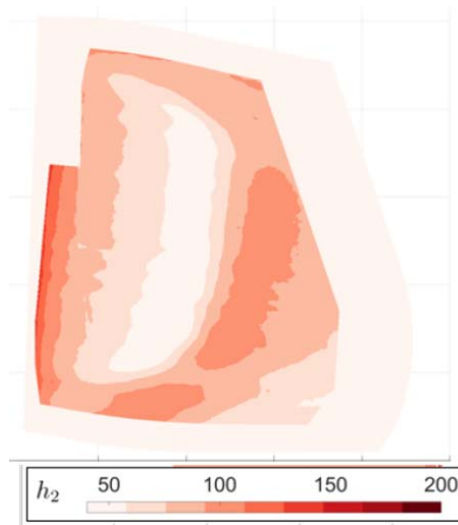


Figure 56. Experimental HTC profile at Suction Side (I. Jonsson V. C., 2020)

To reduce simulations uncertainties and because of the placement of the IRT camera at a certain angle, the experimental contours from (I. Jonsson V. C., 2020) have not captured enough data points near the endwalls and the leading and trailing edge. Despite that, it can be seen that the shapes are close, the high values close to the leading edge are well captured.

At the suction side, the transition is triggered at approximately 40% of the chord for the experimental data (low HTC region), in the numerical results, a similar transition pattern is observed even though the absolute values are not the same.

The two areas with high HTC between mid span and trailing edge are well capture in terms of position, but the shape is different on the simulations. The low HTC area mentioned, and the close to both trailing edge and hub are likely to cause flow separation, and it can trigger an early transition of the boundary layer over the suction side.

HTC
Contour 1
200.0
180.0
160.0
140.0
120.0
100.0
80.0
60.0
40.0
[W m⁻² K⁻¹]

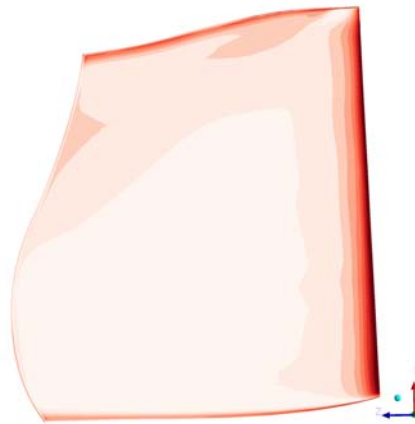


Figure 57. HTC profile at the Pressure Side (Numerical)

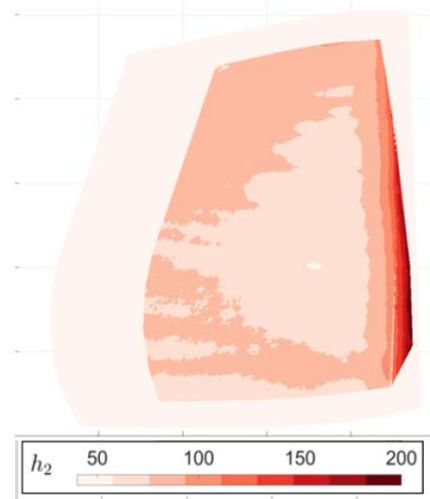


Figure 58. Experimental HTC profile at Pressure Side (I. Jonsson V. C., 2020)

Pressure side high HTC values close to the trailing edge agrees decently, and the same can be said about the big low HTC area in the middle and close to the hub regions. Because of the colorscale on the numerical contour, some accuracy is lost for the lowest values (under $40 \frac{W}{m^2 K}$). Same can be said for the suction side.

Overall, the transition region for the numerical result is in good agreement with the experimental data, but also it should be noted that the HTC distribution over the vane is lower than the experimental data.

5.2.2 Transition onset (aerothermal)

As done on for the aerodynamic evaluation, only the suction side is analyzed, pressure side is out of the scope. The experimental results are compared to the two cases described at the Section 3.6 **Error! Reference source not found.**

5.2.2.1 Suction side

As said before, two numerical simulations were performed. In Figure 59, it is observed that the constant heat flux provides a better estimation in the laminar region. For the constant surface temperature case, the transition region has a huge discrepancy,

although the transition intensity has been captured quite well. Both cases agrees on the fully turbulent region prediction.

None of the suggested simplifications capture the experimental curve. The transition onset location was not captured satisfactorily. Development of a complex heat transfer simulation is suggested as future work, using CFX is should be possible to get a better approach than the actual.

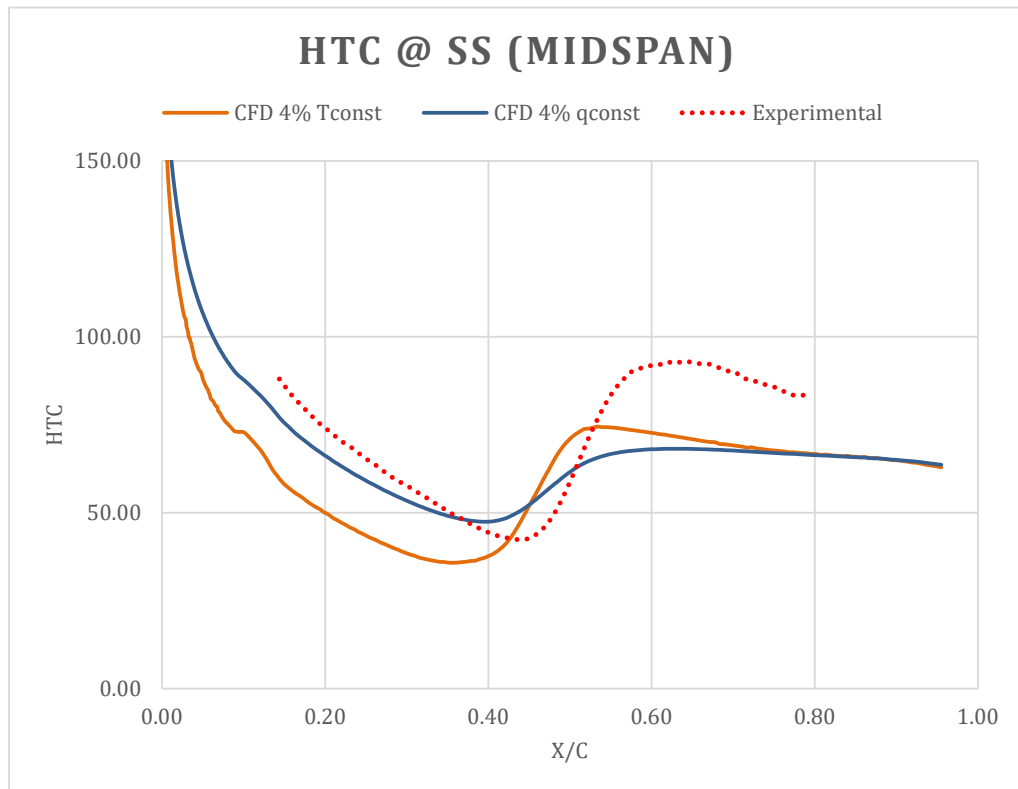


Figure 59. Heat Transfer Coefficient Comparison at Suction Side with Constant wall temperature and constant heat flux on the Blade wall

6 Conclusions

This report exhibits the results of a 6 months project which aim was to validate experimental data of a TRS OGV obtained previously from the Chalmers rig. Both flow parameters and heat transfer were studied. CDF tools were used to simulate the real phenomena, and compare these results with the experimental data.

Numerical data was obtain using RANS-CFD with SST $k-\omega$ turbulence model and the Langtry-Menter $\gamma-\theta$ transition model and two different assumptions for the heat transfer (constant blade temperature or constant heat flux).

The aerodynamic results were encouraging, most of the numerical flow features match with the experimental data, with some exceptions e.g., overloading of the blade close to hub and shroud. This issues can be related to the use of an unextended model for the mesh, leading to a stiffer mesh and the the overloading close to the walls. This is only an conjecture, future simulations can be done in this field to check the truthfulness of the previous postulation.

Aerothermal result were not as promising as the aerodynamical. Separation transition of the boundary layer was expected at the suction side, and transition onset position was pursued. Heat transfer has an alike distribution over the blade, but the transition onset was not properly capture with none of the 2 models used. A more complex heat transfer modelling is required to fully capture the intricacy of the problem in hand.

The thesis results offers a good base for future works over the OGV structure, for validation of experimental data and for future designs of hydrogen propelled engines.

7 Future work

Because of the time constraint, this study did not cover all the fields that may be interesting, there are a lot of work to do left, the following thoughts are only some of the possibilities that exist to continue with the work and help to increase the knowledge on these phenomena:

1. This project is focused on predicting the transition onset accordingly to experiments, a project focus on transition length is desirable, to complete the transition prediction.
2. Change eddy length scale and turbulent intensity to get a turbulent decay closer to the experimental data.
3. Make a research about how to check thickness momentum Reynolds number and acceleration parameter.
4. Development of a complex heat transfer model to capture the transition onset satisfactorily. Change parameters in CFX such as the coefficients of transport equations of Langtry-Menter γ - θ transition model to increase the complexity of the numerical simulation to capture the conjugate heat transfer coefficient distribution more accurately.

8 Bibliography

- A.A.Torres Sampaio Barros, F. F. (2017). *Use of Gamma Theta Model to Determine the Aerodinamics Characteristics of NACA 23012*. Curitiba: ABCM.
- ANSYS, I. a. (2020). *ANSYS CFX-Solver Theory Guide (2020 R1)*.
- B.Rojo. (2017). *Aerothermal Experimental Investigation of LPT-OGV's*. Gothenburg: PhD Thesis, Chalmers University of Technology.
- Carlos Xisto, I. J. (n.d.). Conceptual Design of a Compressor Vane-HEX for LH2Aircraft Engine Applications.
- CFDSupport. (n.d.). <https://www.cfdsupport.com/OpenFOAM-Training-by-CFD-Support/node339.html>. (CFD Support)
- Chenglong Wang, L. L. (2015). Experimental and numerical investigation of outlet guide vane.
- Denton, J. D. (2010). SOME LIMITATIONS OF TURBOMACHINERY CFD.
- Dhanasegaran, R. (2018). *Experimental and Computational Investigation of Heat Transfer in Aero Engine Outlet Guide Vane (OGV)*.
- (2020). *Hydrogen Powered Aviation: A fact-based study of hydrogen technology*.
- I. Jonsson, S. D. (2020). *Experimental and Numerical Study of Laminar-Turbulent Transition on a Low-Pressure Turbine Outlet Guide Vane*. London: ASME Turbo Expo. Turbomachinery Technical Conference and Exposition.
- I. Jonsson, V. C. (2018). *Surface Roughness Impact on Secondary Flow and Losses in a Turbine Exhaust Casing*. Oslo: ASME Turbo Expo 2018: Turbomachinery Technical Conference and Exposition.
- I. Jonsson, V. C. (2020). *Infrared Thermography Investigation of Heat Transfer on Outlet Guide Vanes in an Engine Exit Module*. International Journal of Turbomachinery, Propulsion and Power.
- I.Jonsson. (2020). *Experimental Aerothermal Study on Internal Jet*. Gothenburg: Thesis for the degree of Licentiate of Engineering, Chalmers University of Technology.
- J.G. Ardila Marín, D. H. (2015). *Comparison and Validation of Turbulence Models in the numerical study if Heat Exchangers*. TECCIENCIA Vol. 10 No. 19., 49-60.
- Jonsson, I. C. (2020). *Infrared Thermography Investigation of Heat Transfer on Outlet Guide Vanes in an Engine Exit Module*. International Journal of Turbomachinery, Propulsion and Power.
- Lienhard, J. (2020). *Heat Transfer in Flat-Plate Boundary Layers: A correlation for Laminar, Transitional and Turbulent Flow*. ASME.
- R.E.Mayle. (1991). *The Role of Laminar-Turbulent Transition in Gas Turbine Engines*. New York: ASME.
- S. Deshpande, I. J. (2019). *Effect of Surface Roughness on Aerodynamic Performance of Turbine Rear Structure*. Phoenix: ASME Turbo Expo 2019: Turbomachinery Technical Conference and Exposition.
- White, F. M. (2011). *Fluid Mecahnics. Seventh Edition*. University of Rhode Island: McGraw-Hill Series in Mechanical Engineering.



CHALMERS
UNIVERSITY OF TECHNOLOGY